A Molecular-Level Study of the Photo-Oxidation of Aqueous Phase Guaiacyl Acetone in the Presence of ³C*: Formation of Brown Carbon Products

Maria V. Misovich, ¹ Anusha Priyadarshani Silva Hettiyadura, ¹ Wenqing Jiang, ³ Qi Zhang, ³ Alexander Laskin. ^{1,2}*

¹Department of Chemistry, ²Department of Earth and Planetary Sciences, Purdue University, West Lafayette, IN, 47907

³Department of Environmental Toxicology, University of California, Davis, CA 95616

10

15

KEYWORDS. Aqueous SOA, brown carbon, aerosol, UV-vis, liquid chromatography, high-resolution mass spectrometry, mass absorption coefficient, biomass pyrolysis products

20

Manuscript submitted to ACS Earth and Space Chemistry

April 14, 2021

Re-submitted to ACS Earth and Space Chemistry

July 13, 2021

Abstract

30

35

40

45

50

This study examined the effects of simulated solar irradiation on a model system of atmospheric aqueous secondary organic aerosol (aqSOA) formed from oxidation of guaiacyl acetone (GA) by reactions with triplet excited carbon (³C*) generated by photoexcitation of 3,4dimethoxybenzaldehyde (DMB). Both GA and DMB are common components of biomass burning emissions, and their mixture was selected as a case study to investigate the influence of aqueous phase photochemistry on the light absorption properties of atmospheric brown carbon (BrC) pertinent to agSOA formation. Irradiation was performed in a photoreactor designed to mimic sunlight irradiation, and samples were collected at different times of the experiment, which lasted for six hours. Chemical components of samples were separated using high performance liquid chromatography and analyzed with a photodiode array detector and Orbitrap mass spectrometer operated simultaneously to record both UV-visible and high-resolution mass spectra. This allowed us to obtain molecular characterization of the aqSOA individual components as well as information on their light-absorbing properties and how they change over time when irradiated. The results indicate three generations of products formed at different stages of the experiment: monomeric products, dimeric products, and less polar aromatic products similar to those formed during oxygen deprived pyrolytic processes. The monomeric and dimeric products result from oxidation reactions initiated by ³C*, while the less polar aromatic products form as a result of radical recombination. Prior to irradiation, the BrC absorbance is dominated by monomeric species, but it is later dominated by pyrolytic-like products as the monomeric and dimeric products begin to photodegrade. Comparison with previously defined BrC classes based on optical properties suggests that the aqSOA formed in this experiment initially fall outside of these classes but then become more absorbing, consistent with the "very weak" to "weak" BrC classes.

Introduction

55

60

65

70

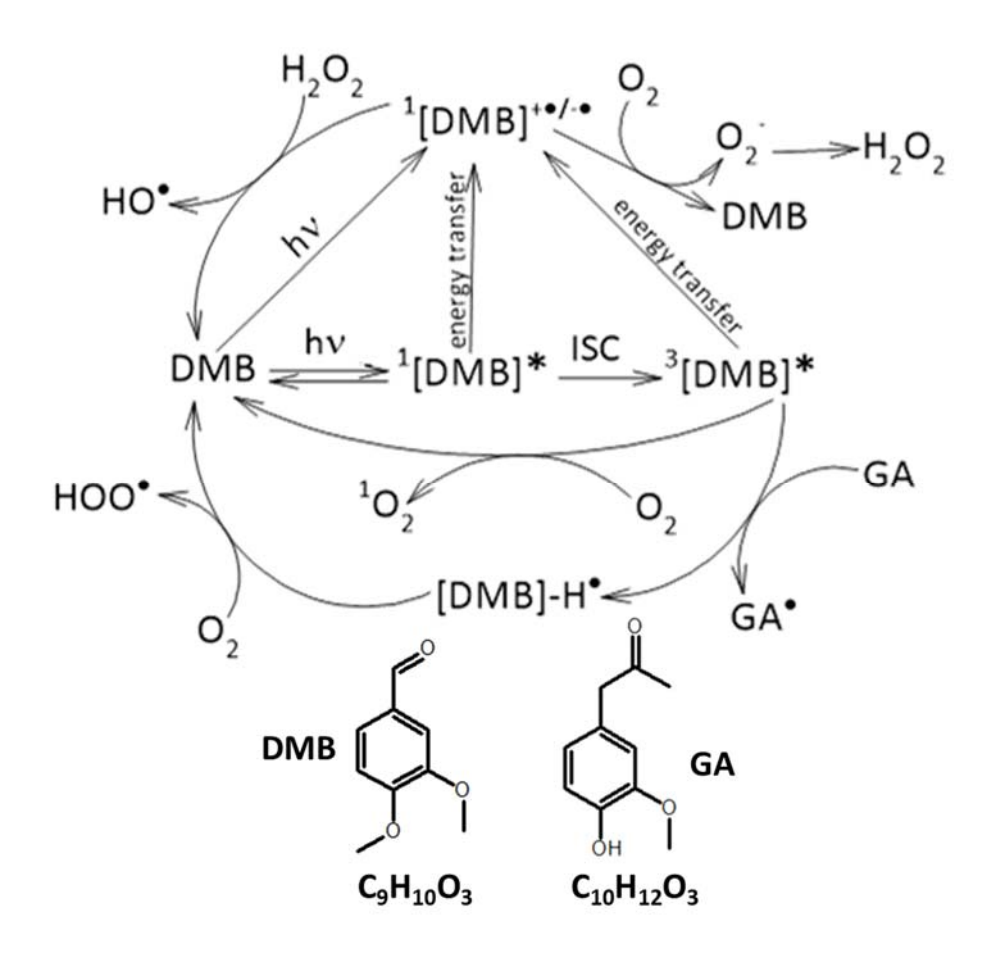
75

80

Biomass burning events, such as forest fires, release many compounds into the atmosphere and are a major contributor to the emissions of light-absorbing organic aerosols collectively termed as atmospheric brown carbon (BrC). BrC strongly absorbs in the UV range, contributes to a sizable fraction of the overall aerosol light absorption, and therefore has implications for climate forcing, air quality, and human health. 1-3 In addition to the direct emissions of primary BrC aerosol, secondary BrC components can be produced through atmospheric aqueous-phase ageing chemistry of fog, cloud droplets and deliquesced particles.⁴ Compounds with high Henry's law constants, including phenols, rapidly partition into aqueous systems such as clouds, fog, and terrestrial water. One such compound is guaiacyl acetone (GA), which is formed as a result of lignin depolymerization during biomass burning.⁵ Its emission rate is between 12-41 µg/g, similar to that of syringaldehyde and sinapyl aldehyde. ⁶ This phenolic compound has a Henry's law constant of 1.19×10^6 and partitions >95% into the aqueous phase under cloud conditions. GA undergoes direct photolysis very slowly compared to phenolic carbonyls in which the carbonyl is directly conjugated to the aromatic ring, with a lifetime greater than 10³ minutes, 8 but it undergoes rapid oxidation reactions in the aqueous phase, leading to the formation of aqueous secondary organic aerosol (aqSOA).9 When oxidized, the compounds in aqSOA undergo additional reactions that yield BrC products and therefore affect optical properties of aged aerosol.⁹ This study aims to characterize the compounds formed when GA is irradiated by sunlight in the presence of oxidizing species and to determine the change in optical properties as a result of irradiation.

Aldehydes are a common component of biomass burning emissions, ⁶ which also partition readily into the aqueous phase. 10 Aldehydes are promoted to their singlet excited state when they absorb UV irradiation, and they can undergo intersystem crossing into a triplet excited state. 11 Triplet excited state carbon (³C*) drives many oxidation reactions and leads to the formation of reactions. 12,13 additional radical compounds, which propagate Specifically, dimethoxybenzaldehyde (DMB), an aromatic aldehyde with methoxy functional groups, is a common compound found in biomass burning emissions. 14 DMB has been found to be the best model compound for studying ³C* concentrations in atmospheric water, ¹⁵ and it is used as an oxidant for GA in our study. Ground state DMB absorbs light, promoting it to a singlet excited state (¹[DMB]*). It can then undergo intersystem crossing (ISC) to form ³C* (³[DMB]*), which

oxidizes GA through hydrogen abstraction. It can also react with molecular oxygen to form singlet oxygen. Ground state DMB can also form a diradical charge transfer complex (1 [DMB] $^{+\bullet/-\bullet}$) when it absorbs light, and both the singlet and triplet excited states can form this complex through electron transfer. This complex can undergo quenching reactions with either $H_{2}O_{2}$ leading to formation of OH $^{\bullet}$ radicals or with molecular oxygen producing first a superoxide anion, followed by its $H_{2}O_{2}$ and OH $^{\bullet}$ reaction products. Scheme 1, adapted from Chen et al, 17 illustrates the overall sequence of GA oxidation chemistry initiated by the DMB excited triplet and further propagated by other oxidizers, including peroxy radicals, hydroxy radicals, and superoxide anions, when irradiated.



Scheme 1. Photooxidation reaction sequence¹⁷ initiated by 3,4-dimethoxybenzaldehyde excited triplet state (³[DMB]*), which then oxidizes the guaiacyl acetone (GA), reactant, and promotes formation of a diradical charge transfer complex (¹[DMB]^{+•/-•}) and various oxygencontaining species, forming oxidizing radicals.

Compounds with carbonyl functional groups, such as GA, undergo Norrish photodegradation. Scheme 2 demonstrates the type I Norrish photochemical pathway for GA, which produces an initial pool of carbon radicals. These can then trigger a cascade of radical chain reactions involving dissolved O₂ and organic constituents and release CO, which partitions into the gas phase, lowering the oxygen content of organic products remaining in the aqueous phase. Photo-oxidation reactions and Norrish photochemistry both play a role in the formation of BrC compounds from lignin-derived precursors.

100

105

110

115

120

Scheme 2. Type I Norrish photochemical decomposition of guaiacyl acetone (GA), initiated by photoexcitation and loss of carbon monoxide.

Photo-oxidation reactions ultimately lead to the formation of CO₂, the most oxidized form of carbon.^{20,21} However, dissolved oxygen might be limited in larger aqueous volumes such as surface and terrestrial water, especially after Norrish photoreactions have occurred. Photoreactions in the oxygen-deficient aqueous phase have been shown to undergo a non-oxidative degradation pathway, which often forms pyrolytic-like condensed aromatic products,²² and this reaction pathway has been observed in terrestrial lignin-derived organic matter.²³ These products are often strongly light absorbing due to the conjugated double bonds.

Previous studies⁸ have shown that direct photodegradation of GA is slow compared to other phenolic compounds emitted from wood combustion due to the lack of conjugation between the carbonyl and the aromatic ring. Yu et al²⁴ showed that phenol, guaiacol, and syringol undergo oxidation by ³C* to form oxygenated monomers and oligomers. In this work we show that GA, in the aqueous phase, undergoes oxidation reactions when irradiated in the presence of DMB, resulting in monomeric and dimeric products as well as pyrolytic-like products formed in non-oxidative degradation processes. In our earlier work of Jiang et al,⁹ we reported the aqSOA mass

yield of ~80% in this system and described overall transformations of its chemical composition. This work focuses on molecular characterization of the BrC chromophore products and evaluation of their optical properties.

125 Experimental Methods and Results

130

135

140

145

150

Sample Preparation and Characterization of aqSOA Composition. The aqueous-phase photochemical experiment of the GA oxidation chemistry initiated by ³DMB* has been presented in great detail in Jiang et al⁹. A dark aqueous sample (R₀) was prepared with the following concentrations: 100 µM GA, 5 µM DMB, 10 mg/L sulfuric acid, and 3 mg/L ammonium sulfate. The concentrations of GA and DMB are relevant to the atmospheric aqueous concentrations of phenols and aromatic carbonyls. During wintertime in air masses influenced by wood combustion, measured fog drop concentrations of syringol, guaiacol, and a few of their derivatives in northern California range up to approximately 30 µM.25 However, this study underreports total phenol concentrations because the authors did not measure a number of phenols emitted from wood combustion, including phenol itself and the benzenediols. We chose 100 µM in this study in order to be able to quantitatively measure SOA production and evolution by AMS. Sulfuric acid was added to adjust the pH to 4.6 to mimic cloud and fog waters impacted by wood burning. 15,26-28. Sulfate was used as an internal standard for quantification of aqSOA via aerosol mass spectrometry (AMS). 100 mL of solution was placed in a 110 mL Pyrex tube, capped, continuously magnetically stirred, and irradiated in a Rayonet RPR-200 photoreactor equipped with 2 RPR-3000 bulbs, 7 RPR-3500 bulbs, and 7 RPR-4190 bulbs, which emit wavelengths centered at 300 nm, 350 nm, and 419 nm, respectively. The light flux in the photoreactor roughly simulates sunlight. Detailed discussions on the comparison of the photochemical kinetics in the RPR-200 photoreactor with that in the ambient atmosphere can be found in George et al.²⁹ Samples of the irradiated solutions (P₁, P₂, P₃) were collected at selected time intervals as shown in table 1, and were stored frozen pending offline analysis. Loss of the GA and DMB reactants was monitored using an HPLC pump connected to a photodiode array (PDA) detector(Agilent Technologies Inc.). HPLC separation was performed on a reversed-phase column (Eclipse XDB-C18, 4.6 × 150 mm, 5 μm packing) using 80% Milli-Q water and 20% acetonitrile as the mobile phase at a flow rate of 0.7 mL/min. A detection wavelength of 280 nm was used for both GA and DMB. Online measurements of

aqSOA mass concentration were performed using an aerosol mass spectrometer. The sample solution was atomized and dried to a relative humidity (RH) <5% before being transferred to the AMS. The AMS operated alternatively between "V" and "W" modes (mass resolution $\Delta m/m$ of ~3000 and ~5000, respectively) to acquire mass spectra up to 485 and 280 amu, respectively. The AMS data was processed using the standard AMS data analysis toolkits (SQUIRREL v1.56D and PIKA 1.15D). Elemental ratios and organic mass to organic carbon (OM/OC) ratio for aqSOA products were calculated from AMS data according to the approach reported in Jiang et al. The OM contribution from the initial reactants for R₀ was calculated from the starting concentrations of GA and DMB and the molecular weights of GA and DMB. For P₁, P₂, and P₃, the OM values were calculated as a sum of OM_{reactants} attributed to the remaining reactants (GA and DMB) determined by HPLC-PDA and OMagSOA attributed to agSOA products measured by AMS as described in Jiang et al.⁹ The AMS measurements of the initial solution show negligible organic signals, suggesting that GA and DMB fully evaporated during the atomization and drying processes. Only low volatility agSOA products were measured by the AMS. Thus, the contribution of GA and DMB must be added to the OM value reported by AMS to calculate total OM. OC values were calculated similarly. OC_{reactants} was calculated from OM_{reactants} and the elemental mass fraction of carbon for each reactant, and OCaqSOA was calculated from OMaqSOA and OM/OC. Figure 1 presents a summary of the bulk analysis results describing composition transformations of the GA + ³DMB* → aqSOA photolysis system described in detail in our previous report.⁹ Briefly, panel a shows GA and DMB loss, panel b shows change in agSOA mass concentration and OM/OC, and panel c shows change in O/C and H/C ratios of aqSOA obtained from AMS measurements. Table 1 summarizes collection time of the R₀, P₁, P₂, and P₃ samples analyzed in this work along with their bulk composition characteristics: aqSOA mass concentrations, total OM, OM/OC ratios, fractions of GA remaining, and total OC.

155

160

165

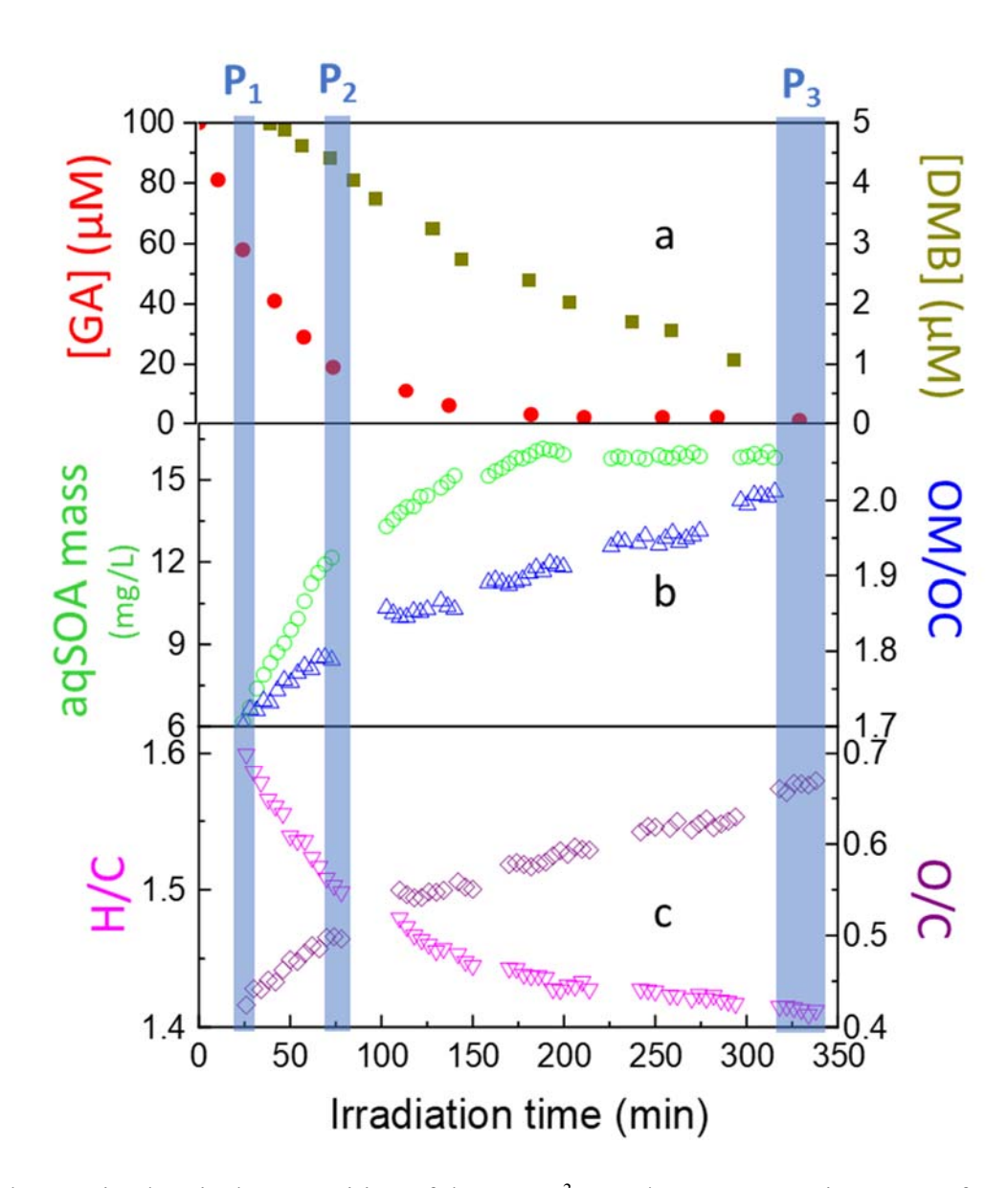


Figure 1. Changes in chemical composition of the $GA + {}^3DMB^* \rightarrow aqSOA$ mixture as a function of reaction (irradiation) time. Individual panels show time-resolved records of (a) GA and DMB concentration, (b) aqSOA mass concentration and OM/OC mass ratio, (c) H/C and O/C elemental ratios of aqSOA. The shaded blue areas indicate periods of time when samples were withdrawn for the chemical characterization presented in this study.

Table 1. Summary of The GA + 3 DMB* \rightarrow aqSOA Samples Investigated in This Study

185

190

195

200

ID	Sample	Collection	aqSOA	Total OM	OM/OC	[GA]/[GA] ₀	Total OC
	Description	time	mass conc.	(mg/L)			(mg/L)
		(min)	(mg/L)				
R_0	GA+DMB reactants	0	1.35	20.20	1.5	1	13.44
P	1 generation products	15-33	5.94	17.16	1.58	0.6	11.22
P ₂	2 generation products	65-82	11.71	15.76	1.76	0.2	9.34
P ₃	3 generation products	313-345	15.82	16.18	1.95	<0.05	8.35

Molecular Characterization. Molecular characterization was performed using a Vanquish high performance liquid chromatography (HPLC) system equipped with a photodiode array (PDA) detector and connected to a QE HF-X Orbitrap high-resolution mass spectrometer (HRMS) with an electrospray ionization (ESI) source (all from Thermo Scientific Inc). Using an autosampler, the aliquots of dark (R₀) and irradiated (P₁, P₂, P₃) samples were injected into a Luna C18 reversed phase column (2 mm × 150 mm, 5 µm particles, 100 Å pores, Phenomenex Inc.) for HPLC-PDA-HRMS analysis. A stepwise gradient elution was performed with a flow rate of 0.2 mL/min using a water/acetonitrile mobile phase doped with 0.1% (v/v) formic acid. The elution proceeded with the following protocol from Lin et al:30 10% acetonitrile at 0-3 min, linear gradient to 90% acetonitrile at 3-63 min, 90% acetonitrile at 63-75 min, linear gradient to 100% acetonitrile at 75-90 min, 100% acetonitrile at 90-100 min, linear gradient back to the initial conditions at 100-101 min, initial conditions at 101-120 min to recondition the column for the next sample run. An injection volume of 15 µL was used. After the HPLC separation, the eluent flow passed through the PDA detector and into the HRMS detector using a parallel connection. UV-visible absorption spectra were measured with the PDA detector over a wavelength range of 200-680 nm at $\lambda \pm 2$ nm resolution. A blank, containing pure LCMS grade water, was analyzed using the same LCMS method as the four samples. Figure 2 shows results of the molecular-level characterization of the individual components identified in the analyzed samples using HPLC-PDA-HRMS platform. The ESI source was operated in an alternating negative/positive mode with a switching frequency of 1.11 Hz. The following conditions were used: spray voltage of 3.51 kV in the positive mode and 2.5 kV in the negative mode, capillary temperature of 250° C, 30 units of sheath gas flow, 10 units of auxiliary gas flow, 1 unit of spare gas flow, and an S-lens RF level of 80 V.

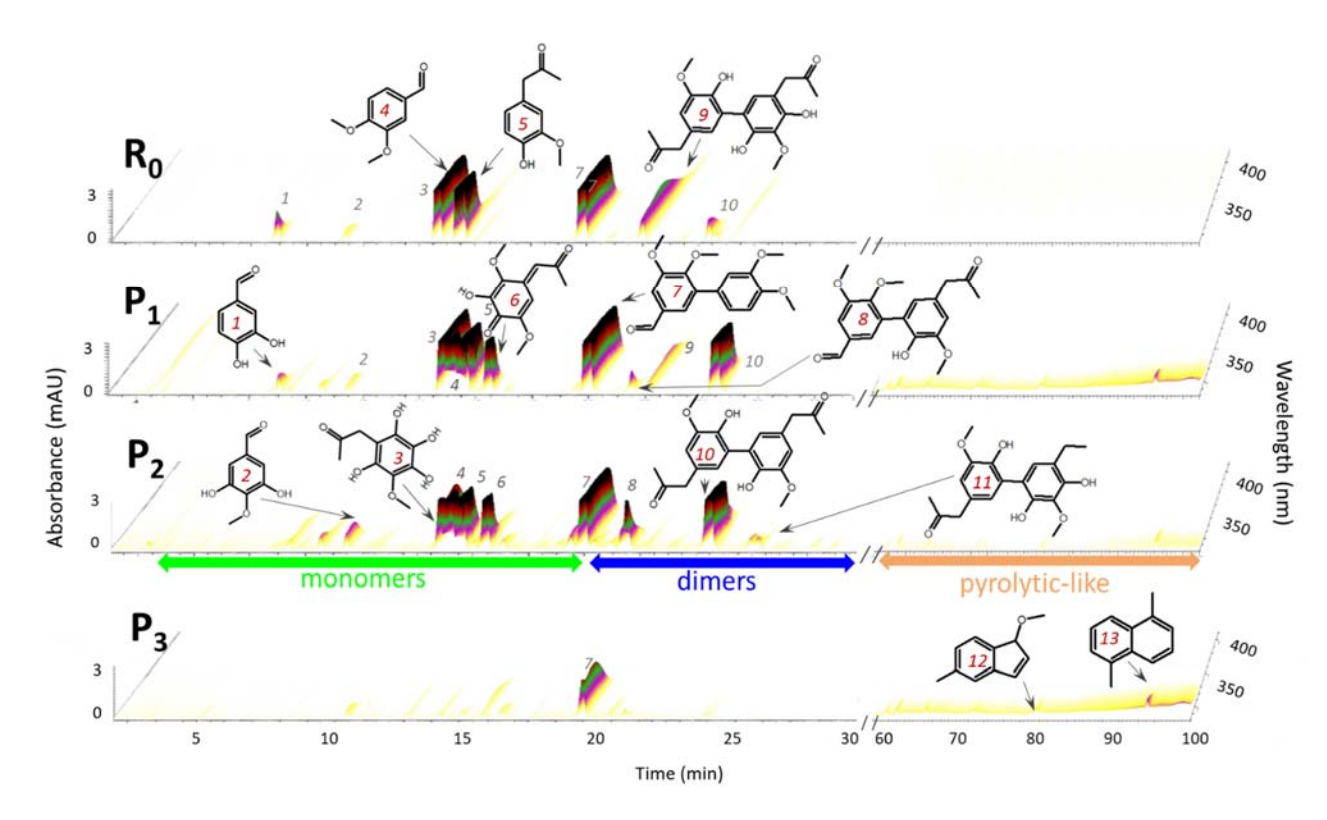


Figure 2. HPLC-PDA chromatograms showing chemical components identified in R₀, P₁, P₂, and P₃ samples. The reaction progress indicates buildup of monomeric and dimeric products, followed by their degradation and the buildup of pyrolytic-like products. Indicated molecular structures of selected species are inferred from correlative analysis of PDA and HRMS data sets included in Table S1. The species are numbered in order of their retention time (RT) appearances. Green, blue, and brown arrows correspond to the RT regions representative of monomers, dimers, and pyrolytic-like products, respectively. The color of the LC-PDA signal corresponds to its intensity, with the following colors listed from least to most intense: yellow, purple, green, red, and black.

HPLC-PDA-HRMS data sets were batch-processed using MZmine software,³¹ which performed peak deconvolution, chromatogram construction, peak smoothing, and peak alignment. HRMS data acquisition was performed at a mass range of *m/z* 80 to 1200 with a mass resolution of 240,000 at 200 *m/z*. For each of the samples, (-)ESI-HRMS spectra were constructed from the deconvoluted data to assess species eluted at 3-30 min, as shown in Figure S1. Formula assignments of HRMS features were assisted by higher-order mass defect analysis using custom

built Excel macros³² followed by formula assignments using the molecular formula calculator (nationalmaglab.org/user-facilities/icr/icr-software). (-)ESI-HRMS data were examined for all four samples at retention times between 3-30 min, as the products eluting during this retention time region are expected to be oxygenated and readily ionized in the (-)ESI mode. Any compounds that were detected in the blank were removed from the data sets for the samples. The initial assignments were limited to the following elemental composition constraints: C \leq 50, H \leq 100, O \leq 50, N \leq 1, S \leq 1. N and S were allowed due to the presence of ammonium sulfate and sulfuric acid in the reaction mixture, as ionic salts may affect the reaction products that occur during photochemical ageing of aqSOA.³³ Formulas without O were not considered. Formulas containing both N and S were excluded, as they are unlikely to occur in our system. Previous studies^{34,35} have shown that sodium formate adduct ions, with the formula [M+HCOONa-H] -, were commonly observed in LC-ESI-HRMS if the LC mobile phase contained formic acid. Thus, for the identified [M-H] - ions, their corresponding [M+(HCOONa)_x-H] - adducts were explicitly searched as the HRMS features differing from their [M-H] - counterparts by the exact masses of (HCOONa)_x = x \times (67.9874 g/mol), whereas x varied between 1 and 3. Additionally, Na was added to the molecular formula calculator parameters to determine whether there were [M+(HCOONa)_x-H] - ions that were not detected in [M-H] form. Na-containing formulas assigned in this manner were only allowed if there were enough C, H, and O atoms to account for a sodium formate adduct and report a neutral formula that matched the criteria used for [M-H]⁻ ions described above. Species that were detected in both [M-H] - and [M+(HCOONa)_x-H] - were reported separately. The total intensity for species detected in more than one ionization mode is the sum of the intensities of each detected ion. (+)ESI-HRMS data were examined for the P₃ sample only to assess species eluted at 60-103 min, with explicit focus on the C_xH_yO_z products as will be described in the discussion section below. The formula assignments were constrained to the elemental composition of C \leq 50, H \leq 100, $O \le 50$, $N \le 2$, $Na \le 1$. Large aromatic species (>300 m/z) without oxygen were allowed, as they can be detected in positive mode.³⁶ Two N atoms were allowed, as previous studies showed that ammonia and reduced N-compounds react with oxidized organic species to form Schiff bases and nitrogen-containing aromatics, some of which may contain two or more N atoms.^{37–40} Nitrogencontaining species may also be the result of [M+NH₄]⁺ ionization, as has been reported previously .34,35Na was allowed to account for [M+Na]⁺ ions. S was not allowed, as S-containing products

225

230

235

240

245

most likely contain a sulfate functional group, which would result in species with preferred ionization in negative mode. Of note, only a fraction of HRMS features recorded in (+)ESI mode were unambiguously assigned with the constrains described above. Assignments of additional (+)ESI-HRMS features required consideration of ions containing higher contributions of S and N atoms, which result in multiple assignment options that could not be experimentally distinguished based on the mass resolving power employed in our experiments. All ambiguous assignments were excluded from consideration in this work. In both positive and negative mode, the signal threshold was 10^5 , and only singly charged ions were considered.

The double bond equivalent (DBE) for each assigned neutral formula was calculated using the following equation:

DBE =
$$C - \frac{H}{2} + \frac{N}{2} + 1$$
 (1)

Figure 3 shows the DBE versus number of (C+N) atoms plots of the species assigned using (-)ESI-HRMS in the R_0 , P_1 , P_2 , and P_3 samples. The bottom line of the shaded area represents linear polyenes C_xH_{x+2} with DBE = $0.5 \times C$. These species contain the lowest possible number of double bonds required to form a conjugated system. The middle line represents *cata*-condensed PAHs, ⁴¹ which consist of aromatic rings arranged in a straight line, with DBE = $0.75 \times C - 0.5$. The top line represents fullerene-like carbons with DBE= $0.9 \times C$, ⁴² which indicate the upper limit of DBE for non-functionalized hydrocarbon molecules. These plots were used to elucidate which of the detected products might be potential chromophores. The brown-shaded region represents species with the sufficient number of DBEs to form a conjugated system. Higher DBE value represents a greater possibility of a conjugated π -bond system, which has the ability to absorb light. Thus, any product that falls within the brown-shaded region represents a potential BrC chromophore. However, not every product that falls within this region is guaranteed to be a potential BrC chromophore, as carbonyl and carboxyl groups also contribute to DBE value but may not be directly conjugated to the aromatic ring.

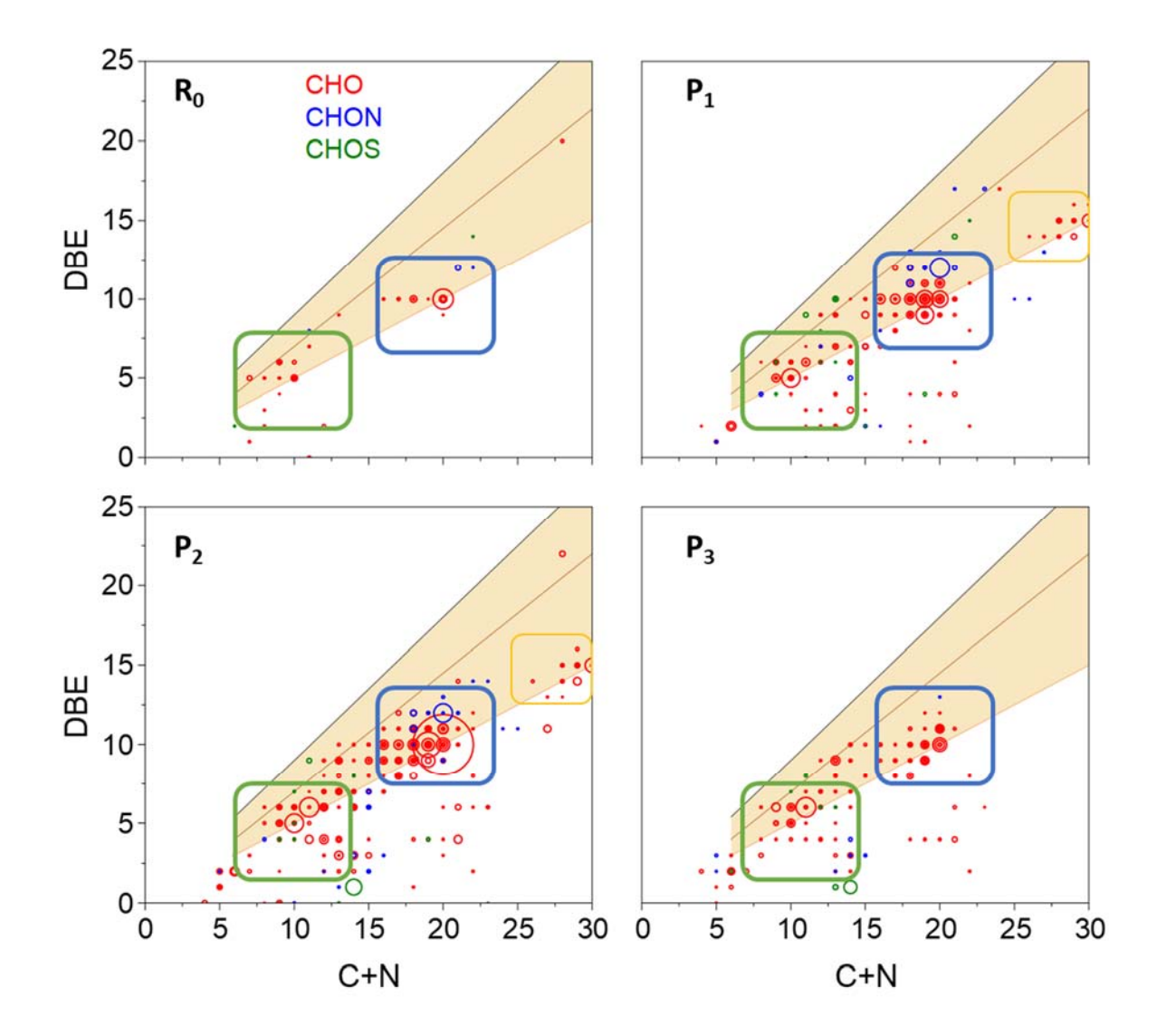


Figure 3. Plots of the double bond equivalent (DBE) vs number of Carbon + Nitrogen atoms of chemical species identified in R₀, P₁, P₂, and P₃ samples. Size of individual symbols are scaled to cubic root of the HRMS signal intensity. The three lines correspond to linear polyenes (bottom line), cata-condensed poly-aromatic hydrocarbons (line in the middle), and fullerene-like compounds (upper line). Species with DBE values inside the shaded region are potential BrC chromophores. Monomeric (outlined in green), dimeric (outlined in blue), and trimeric (outlined in orange) products are observed.

The oxidation state of carbon (OS_C) was calculated for detected species using an equation introduced by Kroll et al^{43,44} for CHO species, modified by Lv et al⁴⁵ to include CHON/S, and further modified to account for the most likely oxidation state of sulfur in our experiment:

$$OS_C = 2 O/C + 3 N/C + 6 S/C - H/C$$
 (2)

Figure 4 shows the OS_C plots for the neutral species assigned using (-)ESI-HRMS in R₀, P₁, P₂, and P₃. An OS_C value of 4 (the most oxidized state) represents CO₂, while a value of -4 (the most reduced state) represents CH₄. OS_C values were plotted against the number of carbon atoms.



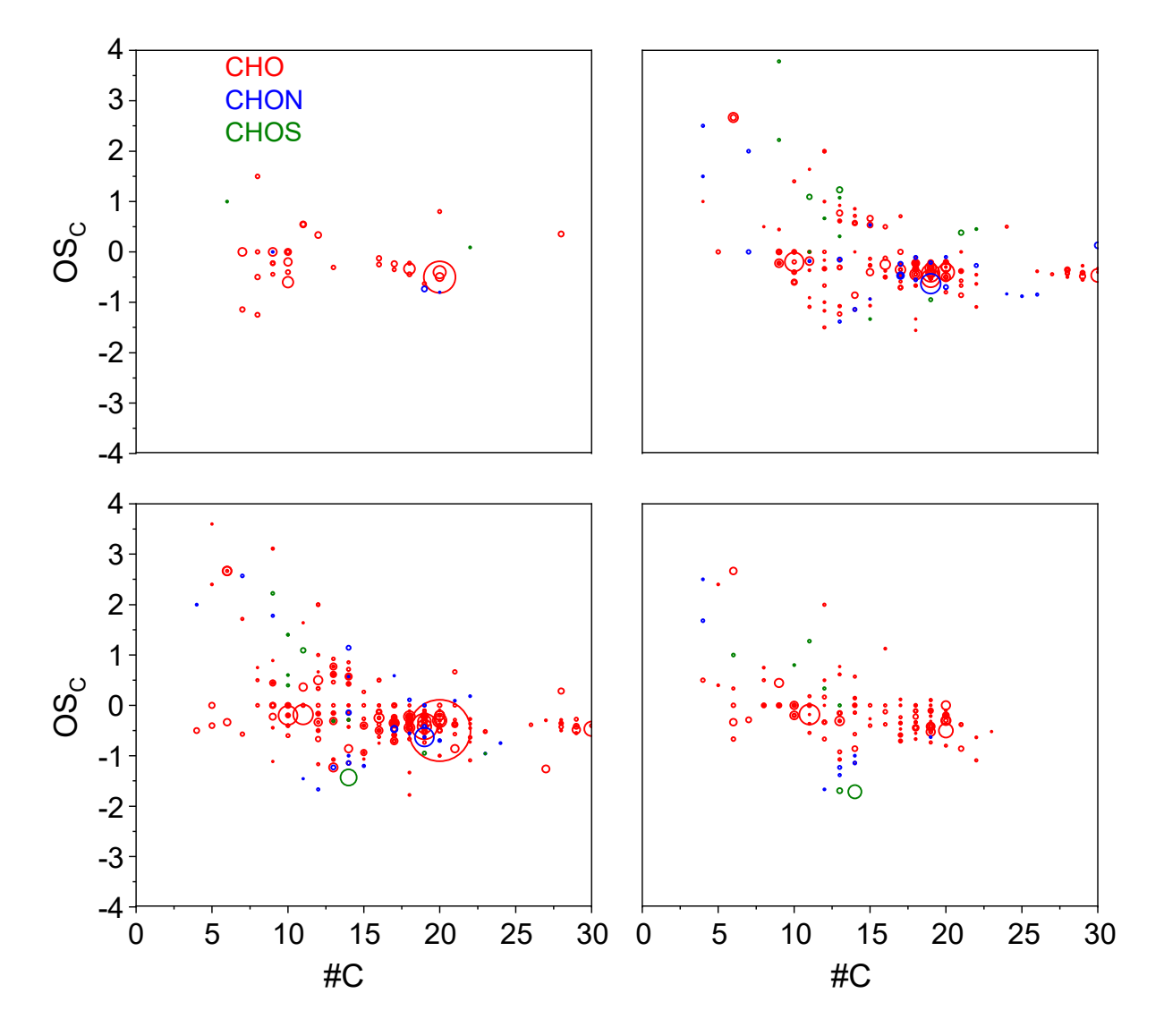


Figure 4. Carbon oxidation state (OS_C) of organic constituents identified in R₀, P₁, P₂, and P₃ samples based on the analysis of (-)ESI-HRMS data. Size of individual symbols are scaled to cubic root of the HRMS signal intensity.

Similarly, Figure 5 shows DBE and OS_C values calculated for neutral species of P₃ detected by (+)ESI-HRMS. All products identified in the aqSOA mixtures based on the assignments of HRMS peaks are summarized in the 'GA+DMB HRMS data.xlsx' file provided in the SI.

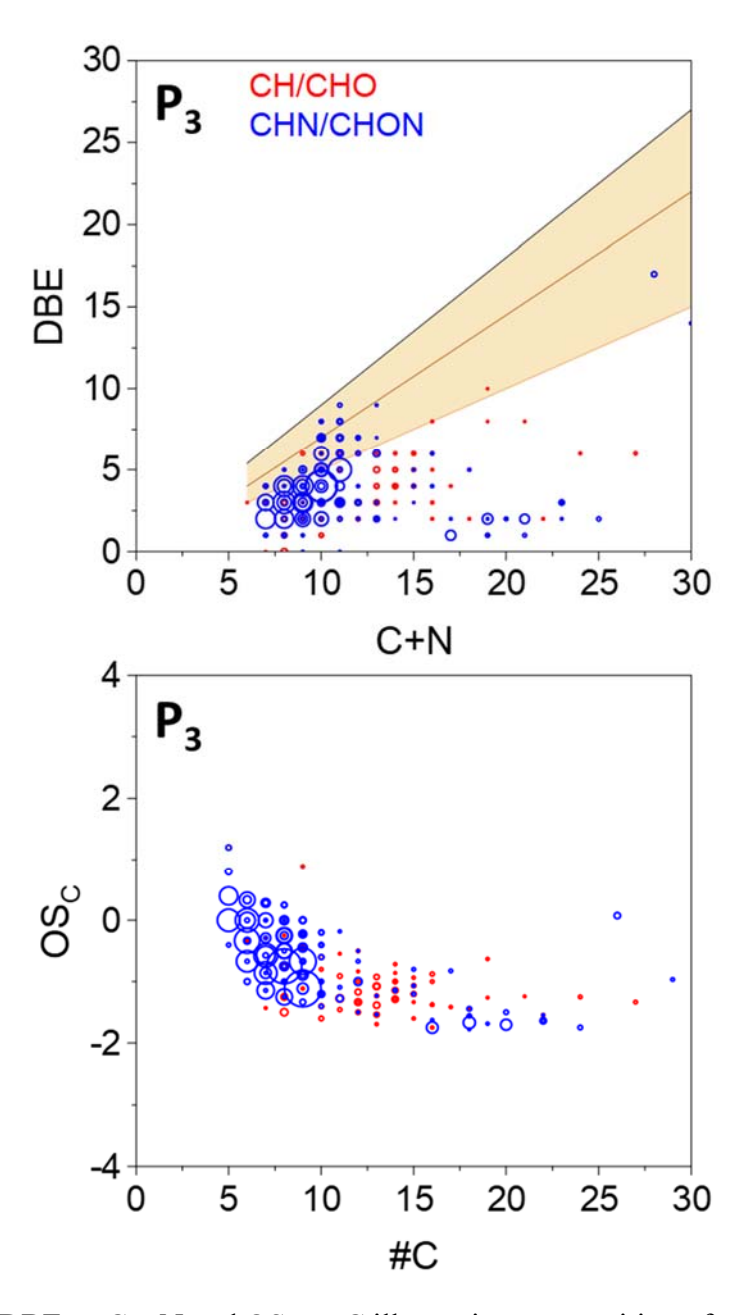


Figure 5. Plots of DBE vs C + N and OSc vs C illustrating composition of pyrolytic-like products detected in P₃ sample based on the analysis of (+)ESI-HRMS data. Size of individual symbols are scaled to cubic root of the HRMS signal intensity.

Photodiode Array Optical Measurements. To measure the overall light absorption characteristics of the R_0 , P_1 , P_2 , and P_3 samples, the samples were injected into the PDA cell from the autosampler without LC separation on a column. The flow rate was 0.2 mL/min, and the mobile phase was kept constant at 55% water and 45% acetonitrile (both doped with 0.1% formic acid) for 3 minutes. The sample was found to elute between 0.14-0.29 minutes. UV-vis absorption spectra were measured in the same manner as in the LC separation method. After flowing through the PDA detector, the samples were directed to a waste container; MS information was not acquired during these runs. Figure S2 shows the column bypass chromatograms for R_0 , P_1 , P_2 , and P_3 , which were used to calculate overall mass absorption coefficients (MAC_λ) for each of the samples.

310

315

320

325

330

335

 MAC_{λ} is a measure of total light absorption by BrC calculated from UV-vis absorbance and mass concentration of OC or OM.¹ Based on the LC-PDA data, we calculate MAC_{λ} using the following equation introduced by Hettiyadura et al⁴⁶ with a modified scaling factor to accommodate the units used in this work.

$$MAC_{\lambda}(\text{m}^{2}\text{g}^{-1}) = \frac{A_{\lambda}(\mu \text{AU sec}) \times F(\text{mL min}^{-1}) \times ln(10)}{l(\text{cm}) \times 60(\text{sec min}^{-1}) \times m_{inj}(\text{g}) \times 10^{10}}$$
(3)

In this expression, A_{λ} is the absorbance value reported by the PDA detector multiplied by the duration of the HPLC-PDA signal as shown in figure S2, F is the LC flow rate, l is the path length, m_{inj} is the mass of the sample injected into the PDA cell, and 10^{10} represents the combined conversion from μ AU to AU, mL to cm³, and from cm² to m². The value of m_{inj} in each sample was calculated by multiplying the OM values listed in Table 1 and the injection volume (15 μ L.)

The fractional contributions of *MAC* attributed to the three product classes shown in figure 2 were also of interest. These were calculated using the following expression:

$$MAC_{\lambda_i} = MAC_{\lambda} \times \left(\frac{I_{\lambda i} \times \Delta t_i}{I_{\lambda} \times \Delta t}\right)$$
 (4)

where, $I_{\lambda i}$ (μ AU) is the averaged absorbance intensity of a BrC component i and Δt_i (min) is its elution time duration, I_{λ} (μ AU) is the averaged absorbance intensity from 3-100 min (Δt = is 97 min), excluding the unretained effluent (0-3 min).

Discussion

340

345

350

355

360

365

Chemical Characterization. As shown in Figure 1, GA concentration decreases over time following the apparent first order kinetics with a rate constant of 0.021 min⁻¹ and a half-life of 32.5 min. DMB concentration decreases linearly over time, suggesting zero order kinetics. aqSOA mass increases over ~200 min of the reaction time and then levels out at later times. However, composition metrics of aqSOA continued to evolve over the entire experiment. Specifically, OM/OC and O/C ratios continued to increase while H/C decreased over the experimental time. This suggests that reactions continue to occur in the condensed phase after aqSOA mass has leveled off and that its constituents continue to evolve. OC values reported by AMS show that total dissolved OC decreases by nearly 40% throughout the experiment, while the values reported by a total organic carbon (TOC) analyzer show only an 11% decrease. This implies that colloids may be forming in the solution. However, this study only reports data for the water soluble fraction.

LC-PDA analysis of the GA+DMB initial mixture (Figure 2) shows two prominent peaks corresponding to the GA (5) and DMB (4) reactants along with DMB and GA dimers (7, 9 and 10) and some minor GA oxidation products (1 and 2) (see 'GA+DMB HRMS data.xlsx') that are likely formed by dark reactions as a result of mixing during transport prior to the irradiation experiment. Proposed structures for these compounds are shown in figure 2, scheme 3, and table S1. These structures are inferred from molecular formulas, PDA signals, and structural and mechanistic data reported by studies on other methoxyphenol molecules. 17,24,47-49 During the first ~90 min of irradiation, the chromatograms for P₁ and P₂ show the buildup of monomeric (C₇-C₁₁) and dimeric (C₁₇-C₂₀) products eluting over 3-30 min and 20-30 min RT periods, respectively. These products are detectable as (-)ESI-HRMS features. Figure 3 shows clusters of species centered at C₁₀ and 5 DBE and C₂₀ and 10 DBE, representing monomeric and dimeric products, in all four samples. Figure 4 shows clusters centered at C₁₀ and C₂₀, both with OS_C values between 0 and -1, suggesting a dimerization reaction pathway. Figure S1 shows clusters of masses corresponding to monomers and dimers. Additionally, the DBE, OSc, and MS plots for P₁ and P₂ show evidence of trimerization, indicated by >26 carbons or m/z >500, as well. This would be less likely to occur in a system without 3C*, as the oxidation rate would be slower, allowing fewer oligomerization reactions to occur.8 Formation of these species is consistent with previous studies of phenolic compounds (e.g. syringol, SYR) irradiated in the presence of ³DMB*. Specifically, the top five

most abundant compounds formed in the SYR + 3 DMB* \rightarrow aqSOA mixtures are monomeric and dimeric products, with the SYR dimer being the most abundant.²⁴ Those products are formed through addition of OH groups to the aromatic ring, exchange of OH and methoxy groups, and ring-opening reactions, ²⁴ analogous to what is observed in the $GA + {}^3DMB^* \rightarrow aqSOA$ system after ~ 90 min of irradiation (samples P₁ and P₂). Following their initial formation, the monomeric and dimeric products undergo photolytic decomposition, and they are largely vanished in the P₃ sample collected after ~310 min of irradiation. A small fraction (4-13%) of CHON and CHOS species are observed in all four samples, with a clear increase observed in irradiated samples. However, these products do not appear to fall into any particular clusters indicative of a specific reaction mechanism. All nitrogen-containing species detected with (–)ESI-HRMS are likely the result of ammonia clustering in the ESI source rather than chemical reactions and are therefore unrelated to aqSOA reactions. Some sulfur-containing species may be organosulfates, as previous studies have shown that organosulfates rapidly form in atmospheric aqueous aerosols from bisulfite ions and formaldehyde,⁵⁰ suggesting that they could also form from sulfuric acid or ammonium sulfate and DMB or any products which also contain an aldehyde group. Organosulfates are detectable with (-)ESI-HRMS.⁵⁰ However, most sulfur-containing species found in this system are likely the result of sulfuric acid clustering in the ESI source, as bisulfite is unstable with respect to sulfate in aqueous solution at room temperature.⁵¹ The low percentage of nitrogen- and sulfur-containing species suggests that ammonium sulfate and sulfuric play a minor, if any, role in the aqueous phase reactions of this system.

370

375

380

385

390

395

Besides monomers and dimers, analyses of P₁, P₂ and P₃ all show formation of additional minor products eluting after 60 min RT, inferred by the elevated PDA signal during this broad retention time region. A fraction of them are identified as less polar aromatic C₅-C₂₄ species detectable with (+)ESI-HRMS. Figure 5 shows species with DBE values that allow for extended conjugated systems and negative-trending OS_C values, indicating that they contain fewer oxygen atoms than those eluting <30 minutes. Those species with few or no oxygen atoms form from Norrish photochemistry after extended irradiation times. A significant fraction (>60%) of the formulas assigned contain one or two nitrogen atoms. Nitrogen-containing species found in this region could be nitrogen containing aromatics, as discussed in previous studies. These species form when ammonia or an amine species reacts with dicarbonyls, resulting in cyclization and loss of one or more water molecules.^{37–40} However, they could also be the result of ammonia clustering

in the ESI source.^{34,35} AMS spectra of the aqSOA show nearly no CHN⁺ or CHON⁺ fragments or an increase in the abundance of N-containing organic ions over the course of irradiation.⁹ Detection of N-containing compounds with LC-PDA-HRMS is likely due to its higher sensitivity towards such compounds. Species that fall within the potential light absorbing region are more likely to be nitrogen containing aromatics, while those that fall below it are likely ammonia clusters.

Scheme 3 shows selected reactions of the GA + ³DMB* chemistry explaining the monomer and dimer products depicted in Figure 2. For clarity, the ID numbers listed for the molecular structures correspond to their order of appearance in Figure 2. The reaction scheme follows an analogous mechanism of Chen et al¹⁷ reported for the oxidation of 4-ethylguaicol by ³DMB*, and several analogs of their system are found in our experiment. While DMB (4) is used as a source of ³C* in this study, several masses are detected that suggest it undergoes reactions with common oxidizing species present in the solution as well. This is supported by figure 1, which shows a decrease in DMB over time. SYR has been found to undergo hydroxyl radical (OH*) addition at a carbon containing a methoxy group followed by methoxy radical (OCH₃*) loss,⁴⁷ resulting in a product differing from the original structure by CH₂. A similar reaction is proposed for DMB. Both methoxy groups in DMB are replaced by hydroxyl groups, forming C₇H₆O₃ (1). This product is only observed at 9.33 min, indicating that only one isomer forms.

Aromatic species can react with ${}^{3}C^{*}$, ${}^{1}O_{2}$, OH*, or OCH₃* to form aromatic radicals, with the radical site delocalized on the aromatic ring, as according to the following four reactions, listed in order of likelihood.

$$R + 3C^* \rightarrow R' + H' \tag{r1}$$

$$R + 10_2 \rightarrow R' + 0_2$$
 (r2)

$$R + OH' \rightarrow R' + H_2O \tag{r3}$$

$$R + OCH_3^{\cdot} \rightarrow R^{\cdot} + CH_3OH \qquad (r4)$$

GA (5), DMB (4), and all aromatic products formed from both precursors are subject to these reactions. Smith et al⁵² reported that, while OH• forms at concentrations up to 9 μM in a system containing 100 μM of a phenolic compound, it oxidizes phenols at a slower rate than ³C*. Chen et al¹⁷ studied ³C*, ¹O₂, and OH• and reported that ³C* was the greatest contributor to 4-ethylguaiacol loss, followed by ¹O₂, suggesting that this may also be true for GA. Thus, the

mechanism explicitly shows GA radicals forming through oxidation by ${}^{3}DMB^{*}$ (r1). However, GA radicals could also form through r2, r3, or r4. OH * and ${}^{1}O_{2}$ both form from the initial reaction with DMB, while OCH $_{3}^{*}$ only forms from methoxy radical loss from GA. Thus, r4 is the least likely reaction pathway.

430

435

After one of the methoxy groups in DMB is replaced by a hydroxy group, it can undergo a radical-forming reaction with ³DMB*, OH*, or OCH₃* to form a new aromatic radical which can then react with OH* to form C₈H₈O₄ (2). This product is only observed between 11.40-11.47 minutes, indicating that only one isomer forms. The OH* likely adds *ortho* to the remaining methoxy groups due to its *ortho*-directing abilities.

$$\begin{array}{c}
 & OH^{\bullet} \\
 & O_{2} \\
 & OH^{\bullet} \\$$

Scheme 3. Proposed reaction mechanism for the irradiated GA+DMB system. Number legends of individual structures correspond to those in Figure 2 and Table S1. Shown molecular structures are the most plausible isomers inferred from correlative analysis of UV-vis and HRMS data, supported by previously reported products in similar systems. ^{17,47,48,53–55}

440

445

450

455

460

465

Following the initial reaction with ³DMB*, GA (5) undergoes radical decomposition to yield H' and GA', where the radical site in the latter is on one of the carbon atoms in the aromatic ring (phenyl radical). Previous studies have shown that phenyl radicals of methoxyphenols can recombine with OH[•] ^{17,47,48} and OCH₃[•] to yield stable monomeric products. ^{47,55} These products can then undergo radical-forming reactions shown in equations r1-r4 with ³DMB*, OH*, or OCH₃* to form new aromatic radicals which can then react with OH or OCH3 to form additional monomeric products. This sequence occurs three times with OH addition to yield C₁₀H₁₂O₆ monomeric products. This product is observed at four elution times of 9.5, 13.0, 14.8 and 15.9 min. As the presented reactions can only form one possible isomer with three new OH groups added to the aromatic ring, the other isomers likely result from one or more OH groups adding to carbon atoms located in the acetone or methoxy functional groups, resulting in a substantially different structure and thus a different retention factor on the column. The highest intensity PDA and HRMS signals for C₁₀H₁₂O₆ are found at 14.8 min, suggesting that this is the most prominent isomer. The proposed structure of C₁₀H₁₂O₆ (3) has three hydroxyl groups added to each previously unoccupied position on the aromatic ring. Consistently, intermediate products of C₁₀H₁₂O₄ and C₁₀H₁₂O₅ composition were also observed in the HRMS data listed in 'GA+DMB HRMS data.xlsx', providing further evidence for this reaction pathway. While previous studies^{47,55} suggested that hydrogen abstraction from benzene ring is the favored pathway for OCH3 reactions, a different pathway can be inferred for the $GA + OCH_3$ reaction. The monomeric product $C_{11}H_{12}O_5$ (6) is proposed to form through two iterations of radical formation followed by radical addition, once with a hydroxyl radical and once with a methoxy radical. This is then followed by hydrogen abstraction and rearrangement of the double bonds to form a quinoidal species. This formula is detected at two elution times: 16.37 and 23.23 min. The earlier elution time, which displays a greater UV-visible signal and MS signal, is likely the quinoidal form, as the increased conjugation enhances absorption.

GA monomeric products (and, to a lesser extent, DMB monomeric products) participate in dimerization reactions. R₁ radicals resulting from the initial reaction of GA with ³DMB* react with one another, forming dimers. Two C₂₀H₂₂O₆ dimers were observed at two elution times, 20.9 and 24.5 min, consistent with the assumption that dimerization may occur through either C-C or C-O coupling of GA monomers. The isomer eluting at 24.5 min displays greater intensity HRMS and PDA signals. Its later elution time suggests that its molecular structure is likely a C-C coupled dimer (10). The other observed isomer is likely a C-O coupled dimer formed through the mechanism suggested in Scheme S1. Additionally, GA radical (R1) reacts with DMB radical (R2) to form the dimeric compound C₁₉H₂₀O₆ (8). Species with this formula are observed at four elution times: 17.04, 19.53, 21.58, and 24.49 mins. The most prominent UV-visible and MS signals are observed at 21.58 min. Previous studies have shown than GA can undergo demethylation, producing an isomer of DMB. This C₉H₁₀O₃ compound could react with GA radical to produce another of the C₁₉H₂₀O₆ isomers.

Majer et al 53 described the formation of a polymer during the photolysis of benzaldehyde by an excited molecule mechanism, suggesting that a similar process could occur for DMB. One prominent photolysis pathway for aromatic aldehydes is the removal of the aldehyde group, resulting in a pair of phenyl and formyl radicals. ⁵⁴ The phenyl radical could react with R2 to form $C_{17}H_{18}O_5$ (7). The $C_{17}H_{18}O_5$ species are observed at three elution times: 20.0, 20.3, and 25.7 minutes. The most prominent MS and UV-visible signals are observed at 20.0 min.

Dimers of C₂₀H₂₂O₇ composition are observed at four elution times: 17.3, 19.5, 22.0, and 30.5 min. These four isomers represent multiple formation pathways that may occur through either C-C or C-O coupling between GA radicals, followed by OH* addition. The signal observed at 22.0 min likely corresponds to C-C coupling forming structure (*10*), followed by OH* addition to form structure (*9*). Another functionalized dimer, C₁₉H₂₂O₆, differs from structure (*9*) by CO, suggesting that it is produced from Norrish photochemical decomposition.¹⁸ The C₁₉H₂₂O₆ species are observed at four elution times: 18.5, 19.0, 23.2, and 26.0 min. The signal observed at 26.0 min, which demonstrates the strongest PDA and MS signals, likely corresponds to a derivative of the dimer formed through C-C coupling (*11*).

The DBE plots display molecular information about all of the assigned compounds, in addition to those explicitly discussed above. The plots show clustering of experimental points

around C₁₀, C₂₀ and C₃₀ corresponding to monomers, dimers and trimers with highest abundances in the P₁ and P₂ irradiated samples, consistent with the proposed mechanism. In the P₃ sample, monomers and dimers are substantially depleted, while trimers, if present, were at concentrations too low to be detected by LC-PDA-HRMS. Species containing fewer carbon atoms than in the monomer (C₁₀) appear in all samples, indicating various fragmentation products that also contribute to the overall reaction pool of aqSOA. In particular, irradiated samples display low DBE products of various sizes, indicating ring-opening and fragmentation chemistry in the GA + ³DMB* system. The most prominent examples are C₁₄H₂₄O₆, C₅H₈O₄, C₆H₁₀O₄, C₁₃H₂₂O₃, C₂₁H₃₆O₉, and C₁₁H₁₆O₁₀. Ring opening and fragmentation reactions have been found to occur in similar systems of 4-ethylguaiacol, ¹⁷ phenol, guaiacol, and syringol, ⁴⁷ which all undergo ringopening oxidation reactions when irradiated in the presence of ³C* and/or other ROS. Ringopening often occurs following the addition of a peroxy radical or singlet oxygen and isomerization to a bicyclic structure and is characterized by a decrease in the H/C ratio and an increase in the O/C ratio. This change is observed for the GA + 3DMB* system at longer irradiation times, as shown by the greater number of compounds with H/C values greater than 1 in P₁-P₃ in figure S3. Thus, figures 3 and S3 both indicate that oligomerization reactions dominate at short (<90 min) irradiation times, while substantial fragmentation and ring-opening reactions occur at longer irradiation times.

500

505

510

515

520

525

In its uncharged form, GA has an oxidation state of carbon (OS_C) of -0.6, and oligomeric products would be expected to have similar OS_C values. Oxidation products would be expected to have higher OS_C values, while ring-opening and fragmentation products would have slightly lower OS_C values. Figure 4 shows OS_C values for individual species detected in each of R₀, P₁, P₂ and P₃ samples. The plots for all 4 samples show a cluster of species with OS_C values between 0 and -1, consistent with oligomerization reaction pathways. However, if only oligomerization reactions occurred in this system, OS_C values would only increase slightly. In contrast, Figure 4 shows that compounds with both higher and lower oxidation states form in the GA + ³DMB* system. Products with OS_C values lower than -1 are not expected to occur in systems where only oxidation takes place. These reduced oxidation state products occur as a result of Norrish photochemistry yielding CO and CO₂ products that degas from the aqueous system. As more oxygen is removed from the system, oxygen-free pyrolytic-like radicals are eventually formed. These react with one another

through radical recombination, eventually forming thermodynamically stable condensed aromatic species with fewer or no oxygen atoms.

530

535

540

545

550

555

Figure 4 shows that P₁-P₃ display a trend towards decomposition products with reduced oxidation states, as is expected for a non-oxidative degradation pathway. The OSc plots for P₁-P₃ demonstrate a greater number of species with negative OSc values than the OSC plot for R₀. Compounds with reduced oxidation states are poorly ionized in (–)ESI-HRMS and therefore might go undetected in this ionization mode. Therefore, we looked into the (+)ESI-HRMS data for additional evidence of pyrolytic-like aromatic products with lower OSc which were shown to be detectable in positive mode.³⁶ Such compounds are also expected to elute later during reversed phase liquid chromatography due to their decreased polarity. Thus, (+)ESI-HRMS data from P₃ sample were further examined for the 60-103 min RT region, which displays a broad, poorly separated PDA signal. Data from this RT region were not examined for the first three samples, as the reactions which form pyrolytic products are not expected to occur on a scale detectable by HRMS until a large amount of oxygen has been removed from the system.

(+)ESI-HRMS reveals products that were not detected with (-)ESI-HRMS. Figure 5 shows the DBE and OS_C plots for the reaction products assigned based on (+)ESI-HRMS data from the 60-103 min RT region shown in figure S4, and figure S5 shows the van Krevelen plot for this region. Most products detected in this region contain 5-15 carbons and have OSc values averaging at approximately -1, O/C ratios <0.5, and H/C ratios varying from 0.5-2.0, consistent with PAH structures. Such products can only form on a scale detectable by HRMS after the high OSc products have photolytically decomposed to yield CO or CO₂ and carbon enriched pyrolytic-like radicals. A mixture of CH/CHO and CHN/CHON compounds are observed, at lower intensities than the masses detected in the 3-30 min range. Nitrogen-containing species with negative OSc values are likely either ammonia clusters^{34,35} or nitrogen-containing aromatics which form from dicarbonyls and amines or ammonia through mechanisms described elsewhere. 1,37-40 Thus, these products also only form after the formation of high OSc products. Pyrolytic-like structures are light absorbing due to their extended conjugated systems. Even at low abundances, such as the concentrations at which they are present in P₁ and P₂, their collective absorbance can potentially contribute a large fraction of the overall absorbance for an oxygen-deficient sample. Detailed mechanisms for the formation of structures 12 and 13 are not apparent. The proposed structures

for C₁₁H₁₂O and C₁₂H₁₂ are chosen for their stability. Mechanisms for the formation of pyrolyticlike products are likely complex and contain many more steps than the mechanism for the formation of monomeric and dimeric products. Formation of pyrolytic-like products also requires a lack of dissolved oxygen in the aqueous phase. Oxygen or oxygen-containing volatile organic compounds (VOCs) can partition into the particle phase, preventing the formation of pyrolyticlike species. However, effective mass accommodation of oxygen into atmospheric particles and droplets is governed by a complex interplay between of gas- and particle-phase processes and is highly influenced by particle size, as reported by Shiraiwa and Poschl.⁵⁶ Thus, oxygen deficiency may be established even at early reaction stages in a bulk sample and pyrolytic-like species are more likely to form in bulk systems or large (>10 µm) droplets than in smaller droplets. However, there are selected scenarios when smaller particles may also become oxygen deficient. For example, mass accommodation coefficients of oxygen and other gases may be significantly limited to surface accommodation even in very small (<1 µm) amorphous and semi-solid particles. Furthermore, mass accommodation coefficients are smaller in higher viscosity particles⁵⁶, suggesting that the formation of pyrolytic-like species may inhibit the intake of oxygen, establishing a feedback loop.

560

565

570

575

580

585

Optical Properties. Relative contributions of different reaction products to the overall BrC properties of the GA + 3DMB* reacting system were evaluated by combining the component-specific HPLC-PDA records. Figure 6 shows the fractionated MAC plots for the four samples. Additionally, absorption angstrom exponent (AAE), which is taken as the slope of $\ln(MAC)$ vs. $\ln(\lambda)$, was calculated for each sample between 280-400 nm and included with the MAC plots. AAE is an essential property for BrC as it defines the wavelength dependence of its absorbance. It has been found to increase with polarity between 250-600 nm, and to be larger when calculated over a shorter wavelength range. It is greater for aerosols collected in biomass burning smoke than for aerosols collected in motor vehicle emissions at wavelengths <600 nm. Hettiyadura et al demonstrated that AAE values measured between 300-500 nm are greater for liquid tar samples generated in oxidative conditions than under pyrolysis conditions. AAE values measured between 330-400 nm have been found to be higher for semi-rural aerosols collected during the winter than during the summer. When calculated between 300-500 nm, BrC extracted from lab-generated soot samples have AAE values averaging at 5.56, while lab-generated liquid tar samples have AAE values ranging from ~13 to ~17. When examining rural aerosols, Li et al erosoted greater

seasonal variation for AAE values calculated between 300-450 nm for water insoluble BrC than water soluble BrC. Chen et al⁶³ reported the highest AAE values between 300-600 nm in the summer for urban aerosols. Water-soluble organic carbon extracts from lab-generated biomass burning samples produced in controlled combustion experiments have AAE values between 300-400 nm ranging from 7.38-8.31.⁶⁴

590

595

600

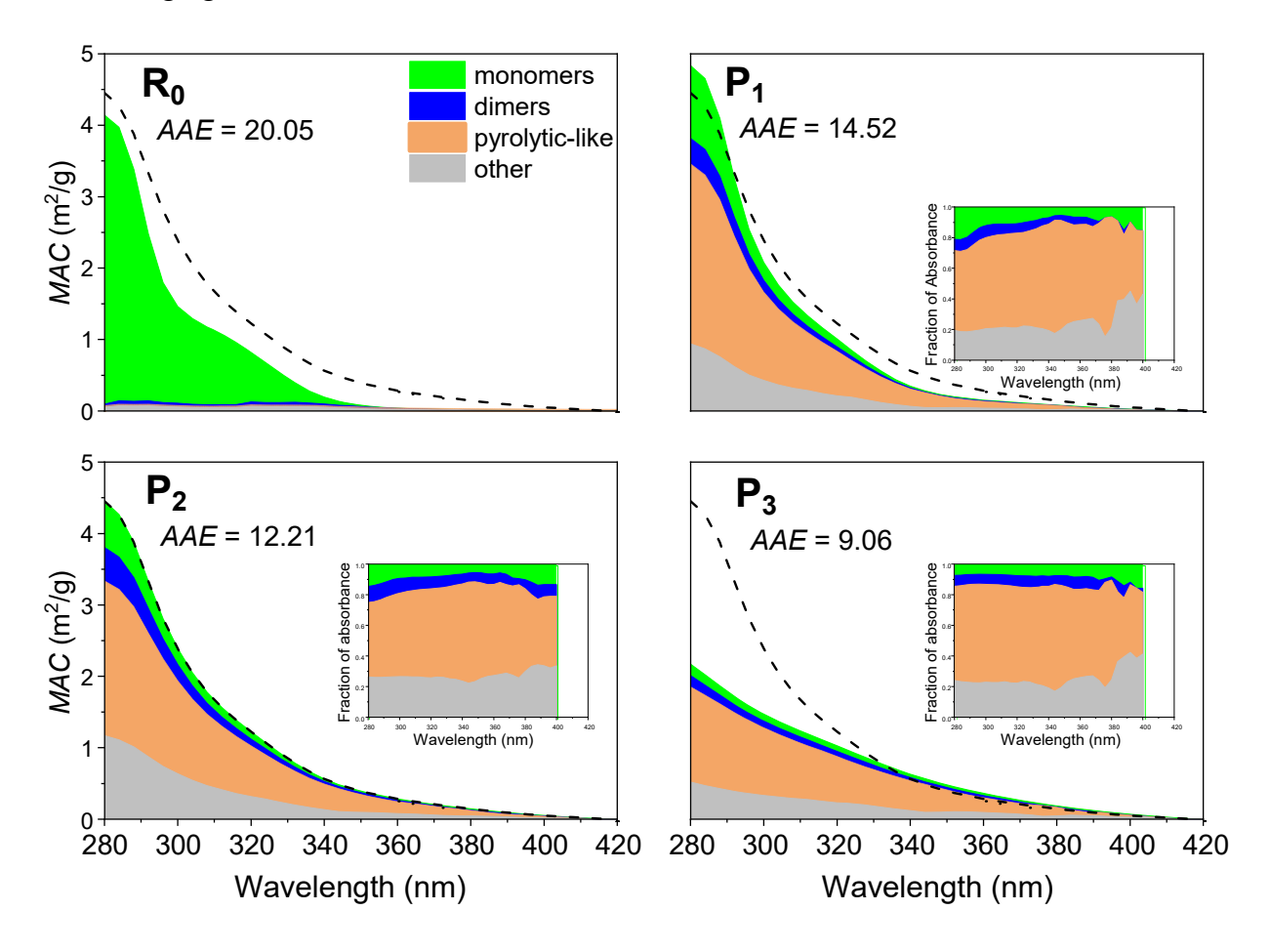


Figure 6. Contributions of different types of products to the overall BrC light absorption of R₀, P₁, P₂, and P₃ samples. The dashed black line is a reference to the highest *MAC* values recorded for P₂ sample. The grey "other" region represents the fraction of absorbance not accounted for by the three major product types. The inset plots show the fraction of absorbance attributed to each product class. These plots only show values between 280 nm and 360 nm for R₀, and between 280 nm and 400 nm for P₁-P₃. At longer wavelengths, the data is too noisy to accurately determine the fraction of absorption for each product class.

In the unreacted R₀ sample, almost all of the BrC absorbance is attributed to the light absorption by GA and DMB reactants, as expected. After irradiation, contribution of monomers

accounts for about 20% of MAC_{λ} in P_1 , while dimeric species contribute about 7%. Notably, pyrolytic-like products contribute ~50% of the overall MAC_{λ} even after the relatively short irradiation time of P_1 . However, they are at too low of a concentration to be detected by HRMS, suggesting that the large fraction of absorbance attributed to pyrolytic-like species is a sum of many strong-absorbing species in low concentrations rather than several prominent light absorbing products. In P_2 sample, monomeric species contribute about 15% of overall MAC_{λ} and dimeric species contribute about 10%, a greater contribution than in P_1 . Pyrolytic-like products contribute ~50% of MAC_{λ} . In P_3 , monomeric and dimeric species each contribute 7% of MAC_{λ} and pyrolytic like species contribute >60%.

At wavelengths below 292 nm, BrC absorbance increases and reaches its maximum in P_1 . Between 292 nm and 324 nm, MAC_{λ} values reach their maximum in P_2 , as indicated by the dashed line on each plot. At later reaction times, P_3 demonstrates nearly 50% decrease in MAC at wavelengths < 324 nm. This is consistent with the trends observed in photodegradation studies of aqueous phenolic carbonyl solutions^{8,65} and photooxidation studies of wood burning samples.⁶⁶ Additionally, the trend has been observed in photooxidation of less polar aromatic BrC samples.⁶⁷

The AAE values for R₀, P₁, P₂, and P₃ are consistent with previously discussed trends⁵⁸ suggesting that it increases with polarity, as R₀, which consists almost entirely of polar species eluting at <20 min, has the highest $AAE_{280-400} \sim 20$, and a decrease to $AAE_{280-400} \sim 9$ is observed as pyrolytic species form in P₁, P₂, and P₃ samples.

There are four classes of BrC introduced by Saleh⁶⁸ with respect to the range of BrC optical properties parameterized in w-k550 space. These classes can be translated to AAE-MAC405 space as demonstrated in previous studies.^{46,61} AAE280-400 for aqSOA samples were plotted against MAC405nm to apportion P₁, P₂ and P₃ samples to the previously defined BrC classes. Figure 7 shows the AAE - MAC405 values calculated for the samples of this study and of selected previous reports, mapped with respect to the four classes of very weak (VW-), weak (W-), medium (M-), and strong (S-) BrC.⁶⁸ Calculation of AAE values from previously reported samples is described in the Supporting Information.

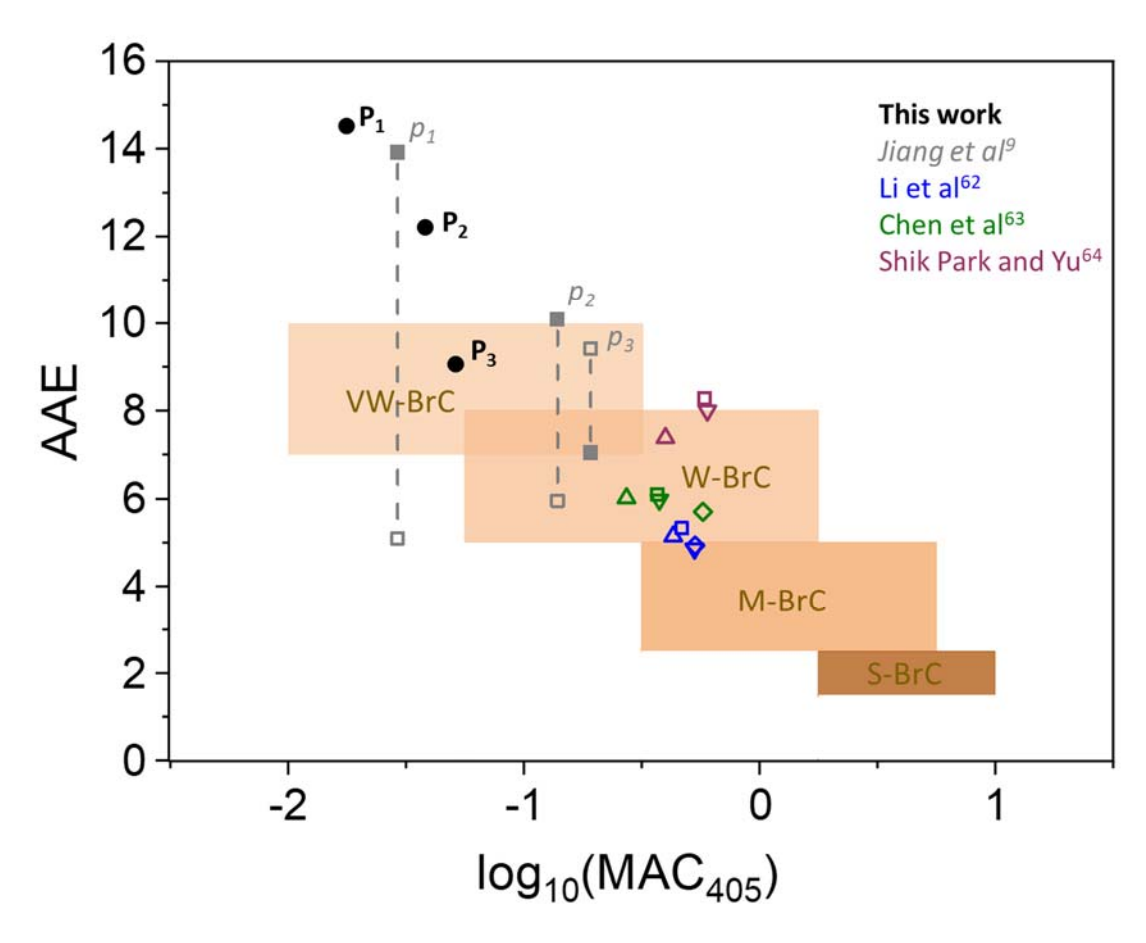


Figure 7. BrC properties of the GA+3DMB* reacting system as reported in this work and by Jiang et al⁹ and selected atmospheric WSOC samples^{62,63} and WSOC extracts from lab-generated biomass burning samples⁶⁴ mapped in the AAE- $log_{10}MAC_{405}$ space following the approach of Saleh. Shaded areas indicate 'very weakly (VW)', 'weakly (W)', 'moderately (M)' and 'strongly (S)' absorbing BrC classes. Data points corresponding to the three irradiated samples are labeled on the plot. The open gray squares represent $AAE_{350-550}$ values reported in Jiang et al,⁹ and the filled gray squares represent $AAE_{280-400}$ values calculated using the same UV-visible datasets. The blue symbols represent water soluble BrC extracted from rural aerosols collected during summer days (square), summer nights (triangle), winter days (inverted triangle), and winter nights (diamond). The green symbols represent water soluble organic matter extracted from urban aerosols collected during spring (square), summer (triangle), fall (inverted triangle), and winter (diamond). The magenta symbols represent water soluble organic carbon extracts from controlled combustion experiments using rice straw (square), pine needle (triangle) and sesame stem (inverted triangle).

Values reported by this work suggest that the AAE280-400 values for the first two irradiated samples fall outside of the four defined BrC classes, while P3 falls within the VW-BrC class. The

log₁₀MAC405 values for P₁, P₂, and P₃ are consistent with the VW-BrC class, with P₃ falling just outside the W-BrC class. However, the values reported by Jiang et al⁹ demonstrate lower AAE values and higher log₁₀MAC₄₀₅ values, placing P₁ in the VW-BrC class and P₂ and P₃ in the overlap between VW-BrC and W-BrC. This discrepancy may be due to different calculation methods; this work calculated AAE from PDA data while Jiang et al⁹ calculated it from UV-visible spectroscopy data. Both studies show that AAE decreases over time and log10MAC405 increases over time. While P₃ demonstrates the lowest MAC values at wavelengths <324 nm, its increase in MAC at longer wavelengths contributes to its lower AAE value. Overall, the $GA + {}^{3}DMB^{*}$ system appears to be less absorbing than typical water soluble organic carbon (WSOC) extracts from rural and urban aerosols reported by Li et al⁶² and Chen et al,⁶³ respectively, as well as those calculated for labgenerated biomass burning samples produced from rice straw, pine needle, and sesame stem in a controlled combustion experiment.⁶⁴ The MAC_{405} values in those three studies^{62–64} are higher than those reported here. This suggests that proxy systems of aqSOA may underestimate the absorptivity of BrC products formed from biomass burning. The greater absorptivity of field samples^{62,63} and lab-generated biomass burning samples⁶⁴ is likely due to greater complexity of the system. This is supported by the AAE280-400 value of P3, which falls within the VW-BrC class. After extended irradiation times, the GA + ³DMB* system becomes more complex and better representative of biomass burning emissions as more products form. As this is a two-component system, it cannot be expected to behave identically to multicomponent systems present in biomass burning aerosols. However, it provides insights into the reactions that would occur in more complex mixtures.

Atmospheric Implications

650

655

660

665

670

675

This study examined the photolytic reactions of a lab proxy system containing compounds found in biomass burning emissions. While it studied a simplified aqueous chemical system, it provided novel mechanistic insights into the multitude of reactions that occur during photochemical processing of aqSOA produced from biomass burning emissions. Specifically, longer irradiation times lead to CO and CO₂ degassing and the formation of pyrolytic-like species in the oxygen-deficient aqueous phase. These species impact the optical properties of aqSOA and may be photo-recalcitrant. Previous studies⁶⁹ have shown that photo-recalcitrant species decelerate photodegradation, increasing the atmospheric lifetimes of BrC molecules by ~30%. O'Brien and

Kroll⁷⁰ demonstrated that the fraction of organic mass present in SOA initially depleted rapidly but leveled off after one day. If the pyrolytic-like species formed in this study are photo-recalcitrant, a feedback loop will be established in which more photo-recalcitrant species form and further extend the lifetimes of BrC species. Additionally, previous studies^{21,71} have demonstrated that aqueous aerosols containing dissolved organic matter undergo an increase in cloud droplet activation efficiency and a decrease in ice crystal nucleation efficiency upon photochemical processing. Dinar et al⁷² reported that aerosols containing a greater fraction of aromatic species demonstrated less efficient cloud activation. Thus, the species formed after longer irradiation times would be expected to result in the formation of fewer clouds. These results suggest that solar irradiation of biomass burning aqSOA could have long-term impacts on weather patterns.

Associated Content

680

685

690

695

700

705

Supporting Information

The Supporting Information is available free of charge.

Figures S1, S2, S3, S4, and S5 report: mass spectra collected between retention times of 3-30 minutes in negative mode, column bypass runs van Krevelen plotss for (-)ESI-HRMS data collected between 3-30 min, a (+)ESI-HRMS mass spectrum collected between 60-103 min, and a van Krevelen plot for (+)ESI-HRMS data collected between 60-103 min, respectively. Table S1 reports the UV-visible spectra, retention time range, neutral formulas, nominal masses and possible structures for the 13 most prominent BrC products detected with HPLC-PDA-HRMS. Scheme S1 shows the formation mechanism for an isomer of the GA dimer product. Appendix A describes how *AAE* values were calculated for referenced studies. A summary of the HRMS data and the molecular assignments is presented in GA+DMB HRMS_SI data.xlsx.

Notes

The authors declare no competing financial interest.

Acknowledgments

This work was supported by the U.S. National Science Foundation, grant no. AGS-1649212 and the California Agricultural Experiment Station (Projects CA-D-ETX-2102-H and CA-D-LAW-6403-RR). PU group acknowledges additional support from discretional startup funds allocated to

A.L. W.J. acknowledges additional funding from the Jastro-Shields Graduate Research Award and the Donald G. Crosby Fellowship at UC Davis.

710

730

735

740

References

- (1) Laskin, A.; Laskin, J.; Nizkorodov, S. A. Chemistry of Atmospheric Brown Carbon. *Chem. Rev.* **2015**, 115 (10), 4335–4382. https://doi.org/10.1021/cr5006167.
- (2) Andreae, M. O.; Gelencser, A. Black Carbon or Brown Carbon? The Nature of Light-Absorbing Carbonaceous Aerosols. *Atmospheric Chem. Phys.* **2006**, *6* (10), 3131–3148. https://doi.org/10.5194/acp-6-3131-2006.
 - (3) Yan, J.; Wang, X.; Gong, P.; Wang, C.; Cong, Z. Review of Brown Carbon Aerosols: Recent Progress and Perspectives. *Sci. Total Enviornment* **2018**, *634*, 1475–1485. https://doi.org/10.1016/j.scitotenv.2018.04.083.
- 720 (4) Geng, X.; Mo, Y.; Li, J.; Zhong, G.; Tang, J.; Jiang, H.; Ding, X.; Naseem Malik, R.; Zhang, G. Source Apportionment of Water-Soluble Brown Carbon in Aerosols over the Northern South China Sea: Influence from Land Outflow, SOA Formation and Marine Emission. *Atmos. Environ.* 2020, 229, 117484. https://doi.org/10.1016/j.atmosenv.2020.117484.
- (5) Simoneit, B. R. T.; Rogge, W. F.; Mazurek, M. A.; Standley, L. J.; Hildemann, L. M.; Cass, G. R.
 725 Lignin Pyrolysis Products, Lignans, and Resin Acids as Specific Tracers of Plant Classes in Emissions from Biomass Combustion. *Environ. Sci. Technol.* 1993, 27 (12), 2533–2541. https://doi.org/10.1021/es00048a034.
 - (6) Nolte, C. G.; Schauer, J. J.; Cass, G. R.; Simoneit, B. R. T. Highly Polar Organic Compounds Present in Wood Smoke and in the Ambient Atmosphere. *Environ. Sci. Technol.* **2001**, *35* (10), 1912–1919. https://doi.org/10.1021/es001420r.
 - (7) McFall, A. S.; Johnson, A. W.; Anastasio, C. Air–Water Partitioning of Biomass-Burning Phenols and the Effects of Temperature and Salinity. *Environ. Sci. Technol.* **2020**, *54* (7), 3823–3830. https://doi.org/10.1021/acs.est.9b06443.
 - (8) Smith, J. D.; Kinney, H.; Anastasio, C. Phenolic Carbonyls Undergo Rapid Aqueous Photodegradation to Form Low-Volatility, Light-Absorbing Products. *Atmos. Environ.* **2016**, *126*, 36–44. https://doi.org/10.1016/j.atmosenv.2015.11.035.
 - (9) Jiang, W.; Misovich, M. V.; Hettiyadura, A. P. S.; Laskin, A.; McFall, A. S.; Anastasio, C.; Zhang, Q. Photosensitized Reactions of a Phenolic Carbonyl from Wood Combustion in the Aqueous Phase Chemical Evolution and Light Absorption Properties of AqSOA. *Environ. Sci. Technol.* 2021. https://doi.org/10.1021/acs.est.0c07581.
 - (10) Allou, L.; El Maimouni, L.; Le Calve, S. Henry's Law Constant Measurements for Formaldehyde and Benzaldehyde as a Function of Temperature and Water Composition. *Atmos. Environ.* **2011**, *45* (17), 2991–2998. https://doi.org/10.1016/j.atmosenv.2010.05.044.
- (11) Ohmori, N.; Suzuki, T.; Ito, M. Why Does Intersystem Crossing Occur in Isolated Molecules of Benzaldehyde, Acetophenone, and Benzophenone? *J. Phys. Chem.* **1988**, *92* (5), 1086–1093. https://doi.org/10.1021/j100316a019.
 - (12) Corral Arroyo, P.; Bartels-Rausch, T.; Alpert, P. A.; Dumas, S.; Perrier, S.; George, C.; Ammann, M. Particle-Phase Photosensitized Radical Production and Aerosol Aging. *Environ. Sci. Technol.* **2018**, 52 (14), 7680–7688. https://doi.org/10.1021/acs.est.8b00329.

- 750 (13) Zepp, R. G.; Schlotzhauer, P. F.; Sink, R. M. Photosensitized Transformations Involving Electronic Energy Transfer in Natural Waters: Role of Humic Substances. *Environ. Sci. Technol.* **1985**, *19* (1), 74–81. https://doi.org/10.1021/es00131a008.
 - (14) Chen, Z.; Anastasio, C. Concentrations of a Triplet Excited State Are Enhanced in Illuminated Ice. *Environ. Sci. Process. Impacts* **2017**, *19* (1), 12–21. https://doi.org/10.1039/C6EM00534A.
- 755 (15) Kaur, R.; Anastasio, C. First Measurements of Organic Triplet Excited States in Atmospheric Waters. *Environ. Sci. Technol.* **2018**, *52* (9), 5218–5226. https://doi.org/10.1021/acs.est.7b06699.
 - (16) Dalrymple, R. M.; Carfagno, A. K.; Sharpless, C. M. Correlations between Dissolved Organic Matter Optical Properties and Quantum Yields of Singlet Oxygen and Hydrogen Peroxide. *Environ. Sci. Technol.* **2010**, *44* (15), 5824–5829. https://doi.org/10.1021/es101005u.
- 760 (17) Chen, Y.; Li, N.; Li, X.; Tao, Y.; Luo, S.; Zhao, Z.; Ma, S.; Huang, H.; Chen, Y.; Ye, Z.; Ge, X. Secondary Organic Aerosol Formation from 3C*-Initiated Oxidation of 4-Ethylguaiacol in Atmospheric Aqueous-Phase. *Sci. Total Enviornment* **2020**, *723*, 137953. https://doi.org/10.1016/j.scitotenv.2020.137953.
- (18) Marchetti, B.; Karsili, T. N. V.; Ashfold, M. N. R. Exploring Norrish Type I and Type II Reactions: An Ab Initio Mechanistic Study Highlighting Singlet-State Mediated Chemistry. *Phys. Chem. Chem. Phys.* **2019**, *23* (26), 14418–14428. https://doi.org/10.1039/C8CP07292B.
 - (19) Norrish, R. G. W.; Appleyard, M. E. S. 191. Primary Photochemical Reactions. Part IV. Decomposition of Methyl Ethyl Ketone and Methyl Butyl Ketone. *J. Chem. Soc. Resumed* **1934**, No. 0, 874–880. https://doi.org/10.1039/JR9340000874.
- 770 (20) Kaplan, L. A.; Cory, R. M. Chapter 6 Dissolved Organic Matter in Stream Ecosystems: Forms, Functions, and Fluxes of Watershed Tea. In *Stream Ecosystems in a Changing Environment*; Academic Press: London, 2016; pp 241–320.

780

- Borduas-Dedekind, N.; Ossola, R.; David, R. O.; Boynton, L. S.; Weichlinger, V.; Kanji, Z. A.;
 McNeill, K. Photomineralization Mechanism Changes the Ability of Dissolved Organic Matter to
 Activate Cloud Droplets and to Nucleate Ice Crystals. *Atmospheric Chem. Phys.* 2019, 19 (19),
 12397–12412. https://doi.org/10.5194/acp-19-12397-2019.
 - (22) Chen, X.; Ye, X.; Chu, W.; Olk, D. C.; Cao, X.; Schmidt-Rohr, K.; Zhang, L.; Thompson, M. L.; Mao, J.; Gao, H. Formation of Char-Like, Fused-Ring Aromatic Structures from a Nonpyrogenic Pathway during Decomposition of Wheat Straw. *J. Agric. Food Chem.* **2020**, *68* (9), 2607–2614. https://doi.org/10.1021/acs.jafc.9b06037.
 - (23) Waggoner, D. C.; Chen, H.; Willoughby, A. S.; Hatcher, P. G. Formation of Black Carbon-like and Alicyclic Aliphatic Compounds by Hydroxyl Radical Initiated Degradation of Lignin. *Org. Geochem.* **2015**, *82*, 69–76. https://doi.org/10.1016/j.orggeochem.2015.02.007.
- Yu, L.; Smith, J.; Laskin, A.; Anastasio, C.; Laskin, J.; Zhang, Q. Chemical Characterization of SOA Formed from Aqueous-Phase Reactions of Phenols with the Triplet Excited State of Carbonyl and Hydroxyl Radical. *Atmospheric Chem. Phys.* **2014**, *14* (24), 13801–13816. https://doi.org/10.5194/acp-14-13801-2014.
 - (25) Sagebiel, J. C.; Seiber, J. N. Studies on the Occurrence and Distribution of Wood Smoke Marker Compounds in Foggy Atmospheres. *Environ. Toxicol. Chem.* **1993**, *12* (5), 813–822. https://doi.org/10.1002/etc.5620120504.
 - (26) Anastasio, C.; Faust, B. C.; Rao, C. J. Aromatic Carbonyl Compounds as Aqueous-Phase Photochemical Sources of Hydrogen Peroxide in Acidic Sulfate Aerosols, Fogs, and Clouds. 1. Non-Phenolic Methoxybenzaldehydes and Methoxyacetophenones with Reductants (Phenols). *Environ. Sci. Technol.* **1996**, *31* (1), 218–232. https://doi.org/10.1021/es960359g.
- 795 (27) Collett, J. L. Jr.; Hoag, K. J.; Sherman, D. E.; Bator, A.; Richards, L. W. Spatial and Temporal Variations in San Joaquin Valley Fog Chemistry. *Atmos. Environ.* **1998**, *33* (1), 129–140. https://doi.org/10.1016/S1352-2310(98)00136-8.

(28) Raja, S.; Raghunathan, R.; Yu, X.-Y.; Lee, T.; Chen, J.; Kommalapati, R. R.; Murugesan, K.; Shen, X.; Qingzhong, Y.; Valsaraj, K. T.; Collett, J. L. Jr. Fog Chemistry in the Texas–Louisiana Gulf Coast Corridor. *Atmos. Environ.* **2008**, *42* (9), 2048–2061. https://doi.org/10.1016/j.atmosenv.2007.12.004.

800

805

835

- (29) George, K. M.; Ruthenburg, T. C.; Smith, J.; Yu, L.; Zhang, Q.; Anastasio, C.; Dillner, A. M. FT-IR Quantification of the Carbonyl Functional Group in Aqueous-Phase Secondary Organic Aerosol from Phenols. *Atmos. Environ.* 2015, 100, 230–237. https://doi.org/10.1016/j.atmosenv.2014.11.011.
- (30) Lin, P.; Fleming, L. T.; Nizkorodov, S. A.; Laskin, J.; Laskin, A. Comprehensive Molecular Characterization of Atmospheric Brown Carbon by High Resolution Mass Spectrometry with Electrospray and Atmospheric Pressure Photoionization. *Anal. Chem.* **2018**, *90* (21), 12493–12502. https://doi.org/10.1021/acs.analchem.8b02177.
- 810 (31) Pluskal, T.; Castillo, S.; Villar-Briones, A.; Oresic, M. MZmine 2: Modular Framework for Processing, Visualizing, and Analyzing Mass Spectrometry-Based Molecular Profile Data. *BMC Bioinformatics* **2010**, *11*, 395–405. https://doi.org/10.1186/1471-2105-11-395.
 - (32) Roach, P. J.; Laskin, J.; Laskin, A. Higher-Order Mass Defect Analysis for Mass Spectra of Complex Organic Mixtures. *Anal. Chem.* **2011**, *83* (12), 4924–4929. https://doi.org/10.1021/ac200654j.
- 815 (33) Klodt, A. L.; Romonosky, D. E.; Lin, P.; Laskin, J.; Laskin, A.; Nizkorodov, S. A. Aqueous Photochemistry of Secondary Organic Aerosol of α-Pinene and α-Humulene in the Presence of Hydrogen Peroxide or Inorganic Salts. *ACS Earth Space Chem.* **2019**, *3* (12), 2736–2746. https://doi.org/10.1021/acsearthspacechem.9b00222.
- Keller, B. O.; Sui, J.; Young, A. B.; Whittal, R. M. Interferences and Contaminants Encountered in
 Modern Mass Spectrometry. *Anal. Chim. Acta* 2008, 627 (1), 71–81.
 https://doi.org/10.1016/j.aca.2008.04.043.
 - (35) Tong, H.; Bell, D.; Tabei, K.; Siegel, M. M. Automated Data Massaging, Interpretation, and e-Mailing Modules for High Throughput Open Access Mass Spectrometry. *J. Am. Soc. Mass Spectrom.* **1999**, *10* (11), 1174–1187. https://doi.org/10.1021/jasms.8b01271.
- 825 (36) Cha, E.; Sook Jeong, E.; Beom Han, S.; Cha, S.; Son, J.; Kim, S.; Bin Oh, H.; Lee, J. Ionization of Gas-Phase Polycyclic Aromatic Hydrocarbons in Electrospray Ionization Coupled with Gas Chromatography. *Anal. Chem.* **2018**, *90* (6), 4203–4211. https://doi.org/10.1021/acs.analchem.8b00401.
- Updyke, K. M.; Nguyen, T. B.; Nizkorodov, S. A. Formation of Brown Carbon via Reactions of
 Ammonia with Secondary Organic Aerosols from Biogenic and Anthropogenic Precursors. *Atmos. Environ.* 2012, 63, 22–31. https://doi.org/10.1016/j.atmosenv.2012.09.012.
 - (38) Bones, D. L.; Henricksen, D. K.; Mang, S. A.; Gonsior, M.; Bateman, A. P.; Nguyen, T. B.; Cooper, W. J.; Nizkorodov, S. A. Appearance of Strong Absorbers and Fluorophores in Limonene-O3 Secondary Organic Aerosol Due to NH4+-mediated Chemical Aging over Long Time Scales. *J. Geophys. Res. Atmospheres* **2010**, *115* (D5), D05203. https://doi.org/10.1029/2009JD012864.
 - (39) Laskin, J.; Laskin, A.; Nizkorodov, S. A.; Roach, P.; Eckert, P.; Gilles, M. K.; Wang, B.; Lee, H. J. (Julie); Hu, Q. Molecular Selectivity of Brown Carbon Chromophores. *Environ. Sci. Technol.* **2014**, 48 (20), 12047–12055. https://doi.org/10.1021/es503432r.
 - (40) Laskin, J.; Laskin, A.; Roach, P. J.; Slysz, G. W.; Anderson, G. A.; Nizkorodov, S. A.; Bones, D. L.; Nguyen, L. Q. High-Resolution Desorption Electrospray Ionization Mass Spectrometry for Chemical Characterization of Organic Aerosols. *Anal. Chem.* 2010, 82 (5), 2048–2058. https://doi.org/10.1021/ac902801f.
 - (41) Siegmann, K.; Sattler, K. Formation Mechanism for Polycyclic Aromatic Hydrocarbons in Methane Flames. *J. Chem. Phys.* **2000**, *112* (2), 698–709. https://doi.org/10.1063/1.480648.

845 (42) Lobodin, V. V.; Marshall, A. G.; Hsu, C. S. Compositional Space Boundaries for Organic Compounds. *Anal. Chem.* **2012**, *84* (7), 3410–3416. https://doi.org/10.1021/ac300244f.

850

860

- (43) Kroll, J. H.; Donahue, N. M.; Jimenez, J. L.; Kessler, S. H.; Canagaratna, M. R.; Wilson, K. R.; Altieri, K. E.; Mazzoleni, L. R.; Wozniak, A. S.; Bluhm, H.; Mysak, E. R.; Smith, J. D.; Kolb, C. E.; Worsnop, D. R. Carbon Oxidation State as a Metric for Describing the Chemistry of Atmospheric Organic Aerosol. *Nat. Chem.* 2011, 3, 133–139. https://doi.org/10.1038/nchem.948.
- (44) Kroll, J. H.; Lim, C. Y.; Kessler, S. H.; Wilson, K. R. Heterogeneous Oxidation of Atmospheric Organic Aerosol: Kinetics of Changes to the Amount and Oxidation State of Particle-Phase Organic Carbon. J. Phys. Chem. A 2015, 119 (44), 10767–10783. https://doi.org/10.1021/acs.jpca.5b06946.
- 855 (45) Lv, J.; Zhang, S.; Luo, L.; Cao, D. Solid-Phase Extraction-Stepwise Elution (SPE-SE) Procedure for Isolation of Dissolved Organic Matter Prior to ESI-FT-ICR-MS Analysis. *Anal. Chim. Acta* **2016**, *948*, 55–61. https://doi.org/10.1016/j.aca.2016.10.038.
 - (46) Hettiyadura, A. P. S.; Garcia, V.; Li, C.; West, C. P.; Tomlin, J.; He, Q.; Rudich, Y.; Laskin, A. Chemical Composition and Molecular-Specific Optical Properties of Atmospheric Brown Carbon Associated with Biomass Burning. *Environ. Sci. Technol.* **2021**, *55* (4), 2511–2521. https://doi.org/10.1021/acs.est.0c05883.
 - Yee, L. D.; Kautzman, K. E.; Loza, C. L.; Schilling, K. A.; Coggon, M. M.; Chhabra, P. S.; Chan, M. N.; Chan, A. W. H.; Hersey, S. P.; Crounse, J. D.; Wennberg, P. O.; Flagan, R. C.; Seinfeld, J. H. Secondary Organic Aerosol Formation from Biomass Burning Intermediates: Phenol and Methoxyphenols. *Atmospheric Chem. Phys.* 2013, 13 (16), 8019–8043. https://doi.org/10.5194/acp-13-8019-2013.
 - (48) He, L.; Schaefer, T.; Otto, T.; Kroflic, A.; Herrmann, H. Kinetic and Theoretical Study of the Atmospheric Aqueous-Phase Reactions of OH Radicals with Methoxyphenolic Compounds. *J. Phys. Chem. A* **2019**, *123* (36), 7828–7838. https://doi.org/10.1021/acs.jpca.9b05696.
- (49) Huang, D. D.; Zhang, Q.; Cheung, H. H. Y.; Yu, L.; Zhou, S.; Anastasio, C.; Smith, J. D.; Chan, C. K.
 Formation and Evolution of AqSOA from Aqueous-Phase Reactions of Phenolic Carbonyls:
 Comparison between Ammonium Sulfate and Ammonium Nitrate Solutions. *Environ. Sci. Technol.* 2018, 52 (16), 9215–9224. https://doi.org/10.1021/acs.est.8b03441.
- (50) Hettiyadura, A. P. S.; Stone, E. A.; Kundu, S.; Baker, Z.; Geddes, E.; Richards, K.; Humphry, T.
 875 Determination of Atmospheric Organosulfates Using HILIC Chromatography with MS Detection.
 Atmospheric Meas. Tech. 2015, 8 (6), 2347–2358. https://doi.org/10.5194/amt-8-2347-2015.
 - (51) Rickard, D. Chapter 2 Sulfur Chemistry in Aqueous Solutions. In *Sulfidic Sediments and Sedimentary Rocks*; Developments in Sedimentology; Elsevier: Amsterdam, 2012; Vol. 65, pp 31–83.
- 880 (52) Smith, J. D.; Sio, V.; Yu, L.; Zhang, Q.; Anastasio, C. Secondary Organic Aerosol Production from Aqueous Reactions of Atmospheric Phenols with an Organic Triplet Excited State. *Environ. Sci. Technol.* **2014**, *48* (2), 1049–1057. https://doi.org/10.1021/es4045715.
 - (53) Majer, J. R.; Naman, S.-A. M. A.; Robb, J. C. Photolysis of Aromatic Aldehydes. *Trans. Faraday Soc.* **1969**, *65*, 1846–1853. https://doi.org/10.1039/TF9696501846.
- 885 (54) Theodoropoulou, M. A.; Nikitas, N. F.; Kokotos, C. G. Aldehydes as Powerful Initiators for Photochemical Transformations. *Beilstein J. Org. Chem.* **2020**, *16*, 833–857. https://doi.org/10.3762/bjoc.16.76.
- (55) Gomez, N.; Henon, E.; Bohr, F.; Devolder, P. Rate Constants for the Reactions of CH3O with Cyclohexane, Cyclohexene, and 1,4-Cyclohexadiene: Variable Temperature Experiments and Theoretical Comparison of Addition and H-Abstraction Channels. J. Phys. Chem. A 2001, 105 (50), 11204–11211. https://doi.org/10.1021/jp010204h.

- (56) Shiraiwa, M.; Poschl, U. Mass Accommodation and Gas—Particle Partitioning in Secondary Organic Aerosols: Dependence on Diffusivity, Volatility, Particle-Phase Reactions, and Penetration Depth. *Atmospheric Chem. Phys.* **2021**, *21* (3), 1565–1580. https://doi.org/10.5194/acp-21-1565-2021.
- 895 (57) Srinivas, B.; Sarin, M. M. Light Absorbing Organic Aerosols (Brown Carbon) over the Tropical Indian Ocean: Impact of Biomass Burning Emissions. *Environ. Res. Lett.* **2013**, *8* (4), 044042. https://iopscience.iop.org/article/10.1088/1748-9326/8/4/044042.

900

915

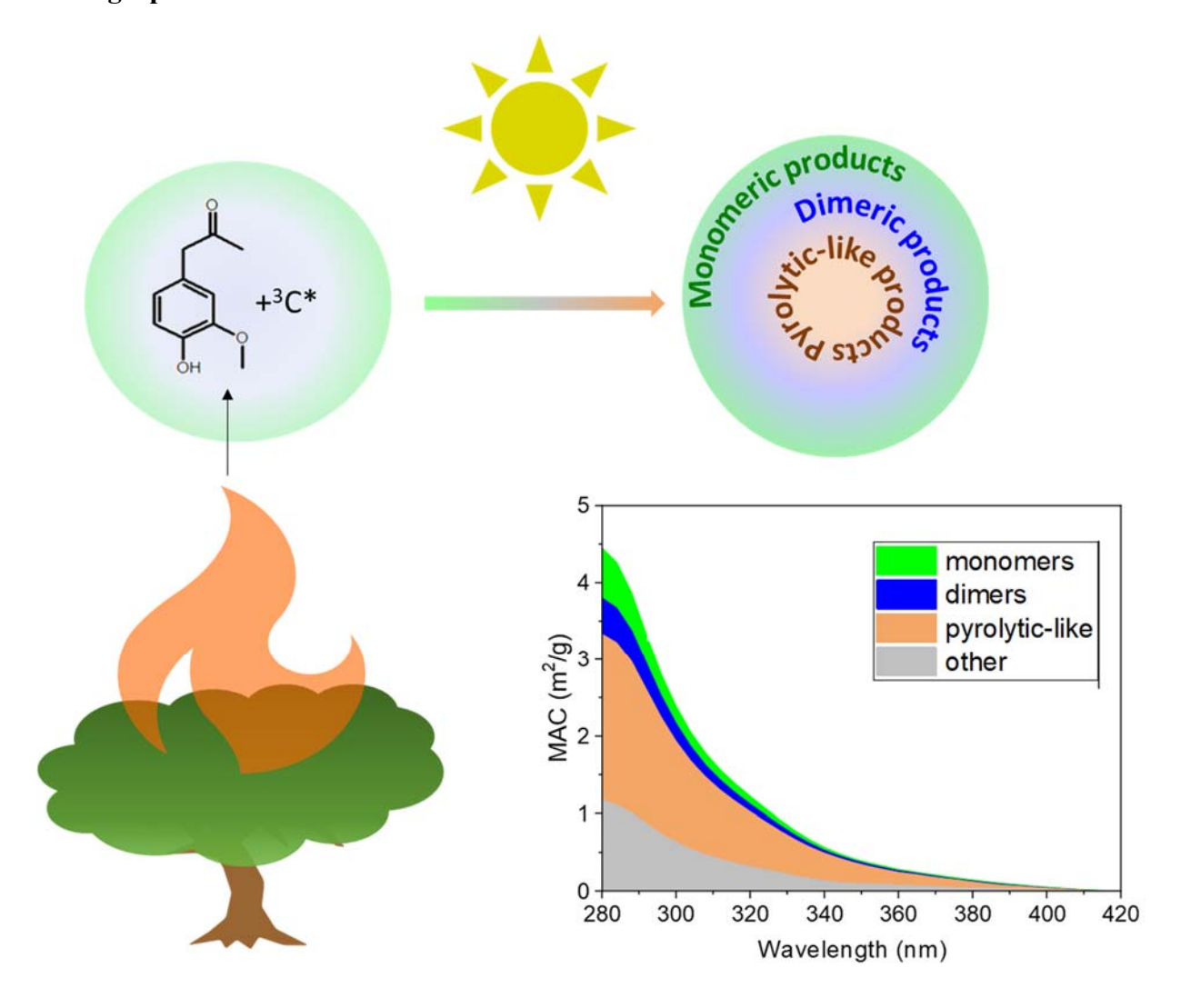
925

- (58) Chen, Q.; Ikemori, F.; Mochida, M. Light Absorption and Excitation—Emission Fluorescence of Urban Organic Aerosol Components and Their Relationship to Chemical Structure. *Environ. Sci. Technol.* **2016**, *50* (20), 10859–10868. https://doi.org/10.1021/acs.est.6b02541.
- (59) Kirchstetter, T. W.; Novakov, T.; Hobbs, P. V. Evidence That the Spectral Dependence of Light Absorption by Aerosols Is Affected by Organic Carbon. *J. Geophys. Res. Atmospheres* **2004**, *109* (D21), D21208. https://doi.org/10.1029/2004JD004999.
- Jiang, H.; Li, J.; Chen, D.; Tang, J.; Cheng, Z.; Mo, Y.; Su, T.; Tian, C.; Jiang, B.; Liao, Y.; Zhang, G.
 Biomass Burning Organic Aerosols Significantly Influence the Light Absorption Properties of Polarity-Dependent Organic Compounds in the Pearl River Delta Region, China. *Environ. Int.* 2020, 144, 106079. https://doi.org/10.1016/j.envint.2020.106079.
- (61) West, C. P.; Hettiyadura, A. P. S.; Darmody, A.; Mahamuni, G.; Davis, J.; Novosselov, I.; Laskin, A. Molecular Composition and the Optical Properties of Brown Carbon Generated by the Ethane
 910 Flame. ACS Earth Space Chem. 2020, 4 (7), 1090–1103. https://doi.org/10.1021/acsearthspacechem.0c00095.
 - (62) Li, J.; Zhang, Q.; Wang, G.; Li, J.; Wu, C.; Liu, L.; Wang, J.; Jiang, W.; Li, L.; Fai Ho, K.; Cao, J. Optical Properties and Molecular Compositions of Water-Soluble and Water-Insoluble Brown Carbon (BrC) Aerosols in Northwest China. *Atmospheric Chem. Phys.* 2020, 20 (8), 4889–4904. https://doi.org/10.5194/acp-20-4889-2020.
 - (63) Chen, Y.; Ge, X.; Chen, H.; Xie, X.; Chen, Y.; Wang, J.; Ye, Z.; Bao, M.; Zhang, Y.; Chen, M. Seasonal Light Absorption Properties of Water-Soluble Brown Carbon in Atmospheric Fine Particles in Nanjing, China. *Atmos. Environ.* **2018**, *187*, 230–240. https://doi.org/10.1016/j.atmosenv.2018.06.002.
- 920 (64) Shik Park, S.; Yu, J. Chemical and Light Absorption Properties of Humic-like Substances from Biomass Burning Emissions under Controlled Combustion Experiments. *Atmos. Environ.* **2016**, 136, 114–122. https://doi.org/10.1016/j.atmosenv.2016.04.022 Get.
 - (65) Tang, S.; Li, F.; Tsona, N. T.; Lu, C.; Wang, X.; Du, L. Aqueous-Phase Photooxidation of Vanillic Acid: A Potential Source of Humic-Like Substances (HULIS). *ACS Earth Space Chem.* **2020**, *4* (6), 862–872. https://doi.org/10.1021/acsearthspacechem.0c00070.
 - (66) Hems, R. F.; Schnitzler, E. G.; Bastawrous, M.; Soong, R.; Simpson, A. J.; Abbatt, J. P. D. Aqueous Photoreactions of Wood Smoke Brown Carbon. *ACS Earth Space Chem.* **2020**, *4* (7), 1149–1160. https://doi.org/10.1021/acsearthspacechem.0c00117.
- (67) Aiona, P. K.; Luek, J. L.; Timko, S. A.; Powers, L. C.; Gonsior, M.; Nizkorodov, S. A. Effect of Photolysis on Absorption and Fluorescence Spectra of Light-Absorbing Secondary Organic Aerosols. *ACS Earth Space Chem.* **2018**, *2* (3), 235–245. https://doi.org/10.1021/acsearthspacechem.7b00153.
 - (68) Saleh, R. From Measurements to Models: Toward Accurate Representation of Brown Carbon in Climate Calculations. *Curr. Pollut. Rep.* **2020**, *6* (2), 90–104. https://link.springer.com/article/10.1007/s40726-020-00139-3.
 - (69) Braman, T.; Dolvin, L.; Thrasher, C.; Yu, H.; Walhout, E. Q.; O'Brien, R. E. Fresh versus Photo-Recalcitrant Secondary Organic Aerosol: Effects of Organic Mixtures on Aqueous Photodegradation of 4-Nitrophenol. *Environ. Sci. Technol. Lett.* 2020, 7 (4), 248–253. https://doi.org/10.1021/acs.estlett.0c00177.

940 (70) O'Brien, R. E.; Kroll, J. H. Photolytic Aging of Secondary Organic Aerosol: Evidence for a Substantial Photo-Recalcitrant Fraction. *J. Phys. Chem. Lett.* **2019**, *10* (14), 4003–4009. https://doi.org/10.1021/acs.jpclett.9b01417.

- (71) Borduas-Dedekind, N.; Nizkorodov, S.; McNeill, K. UVB-Irradiated Laboratory-Generated Secondary Organic Aerosol Extracts Have Increased Cloud Condensation Nuclei Abilities: Comparison with Dissolved Organic Matter and Implications for the Photomineralization Mechanism. *Chimia* **2020**, *74* (3), 142–148. https://doi.org/10.2533/chimia.2020.142.
- (72) Dinar, E.; Taraniuk, I.; Graber, E. R.; Katsman, S.; Moise, T.; Anttila, T.; Mentel, T. F.; Rudich, Y. Cloud Condensation Nuclei Properties of Model and Atmospheric HULIS. *Atmospheric Chem. Phys.* **2006**, *6* (9), 2465–2482. https://doi.org/10.5194/acp-6-2465-2006.

TOC graphic



Supplemental information for:

A Molecular-Level Study of the Photo-Oxidation of Aqueous Phase Guaiacyl Acetone in the Presence of ³C*: Formation of Brown Carbon Products

Maria V. Misovich¹, Anusha Priyadarshani Silva Hettiyadura¹, Wenqing Jiang², Qi Zhang², Alexander Laskin.^{1,*}.

Table of contents

- Figure S1. Mass spectra collected using (–)ESI-MS between 3-30 minutes for all samples
- Figure S2. Column bypass signals for all samples
- Figure S3. Van Krevelen plots for formulas assigned using (–)ESI-MS for all samples
- Figure S4. Mass spectra collected using (+)ESI-MS between 60-103 minutes for P₃
- Figure S5. Van Krevelen plot for formulas assigned using (+)ESI-MS for P₃
- Table S1. UV-visible spectra, assigned chemical formulas, proposed structures, and proposed mechanisms for 13 BrC features
- Scheme S1. Mechanism for GA dimers formed through C-O coupling

Appendix A. Calculation of AAE values from other studies

References

¹ Department of Chemistry, Purdue University, West Lafayette, IN, 47907

² Department of Environmental Toxicology, University of California, Davis, CA 95616

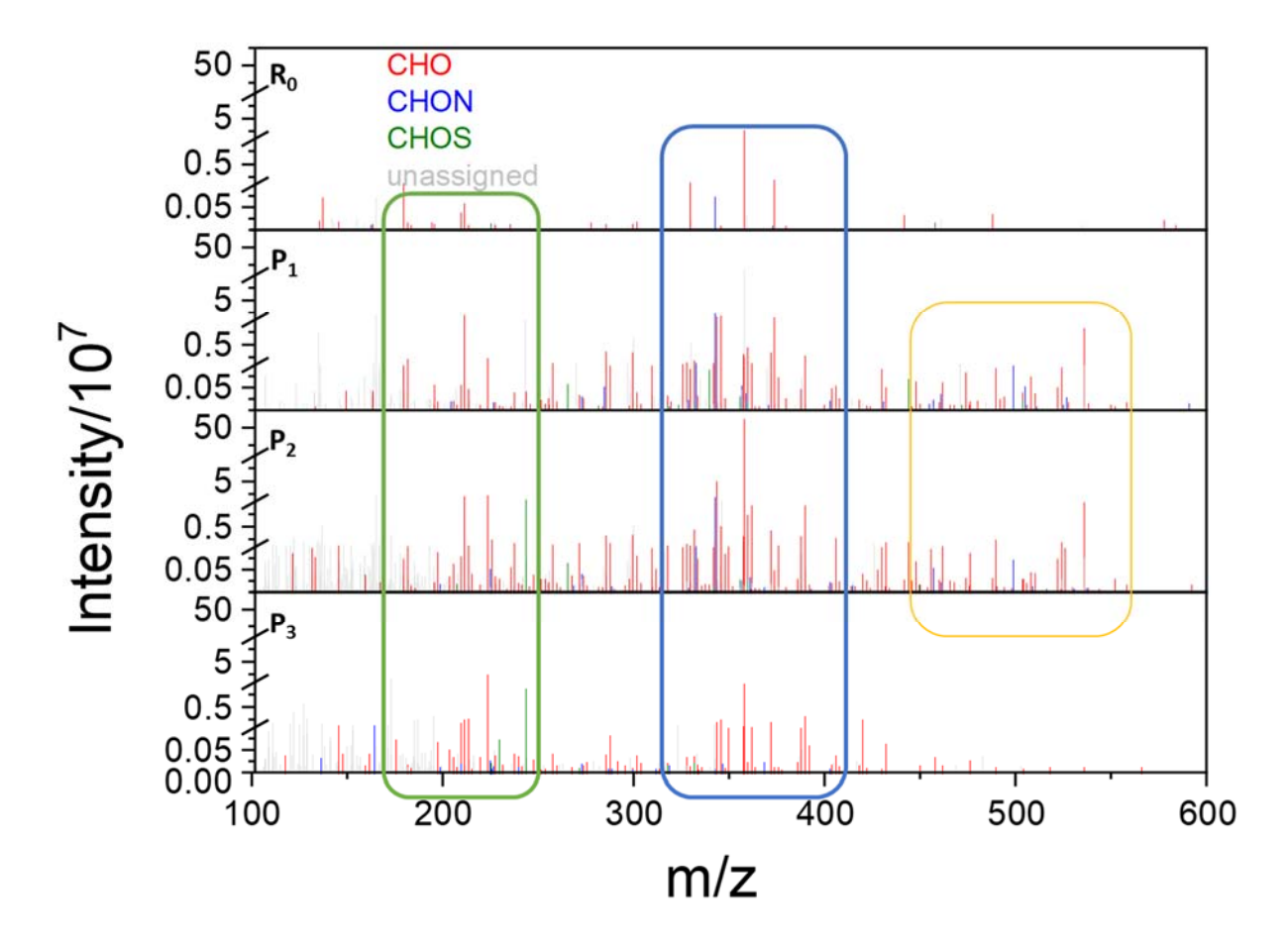


Figure S1. Negative mode mass spectra collected between 3-30 minutes for R₀, P₁, P₂, and P₃. Monomeric (outlined in green), dimeric (outlined in blue), and trimeric (outlined in orange) products are observed.

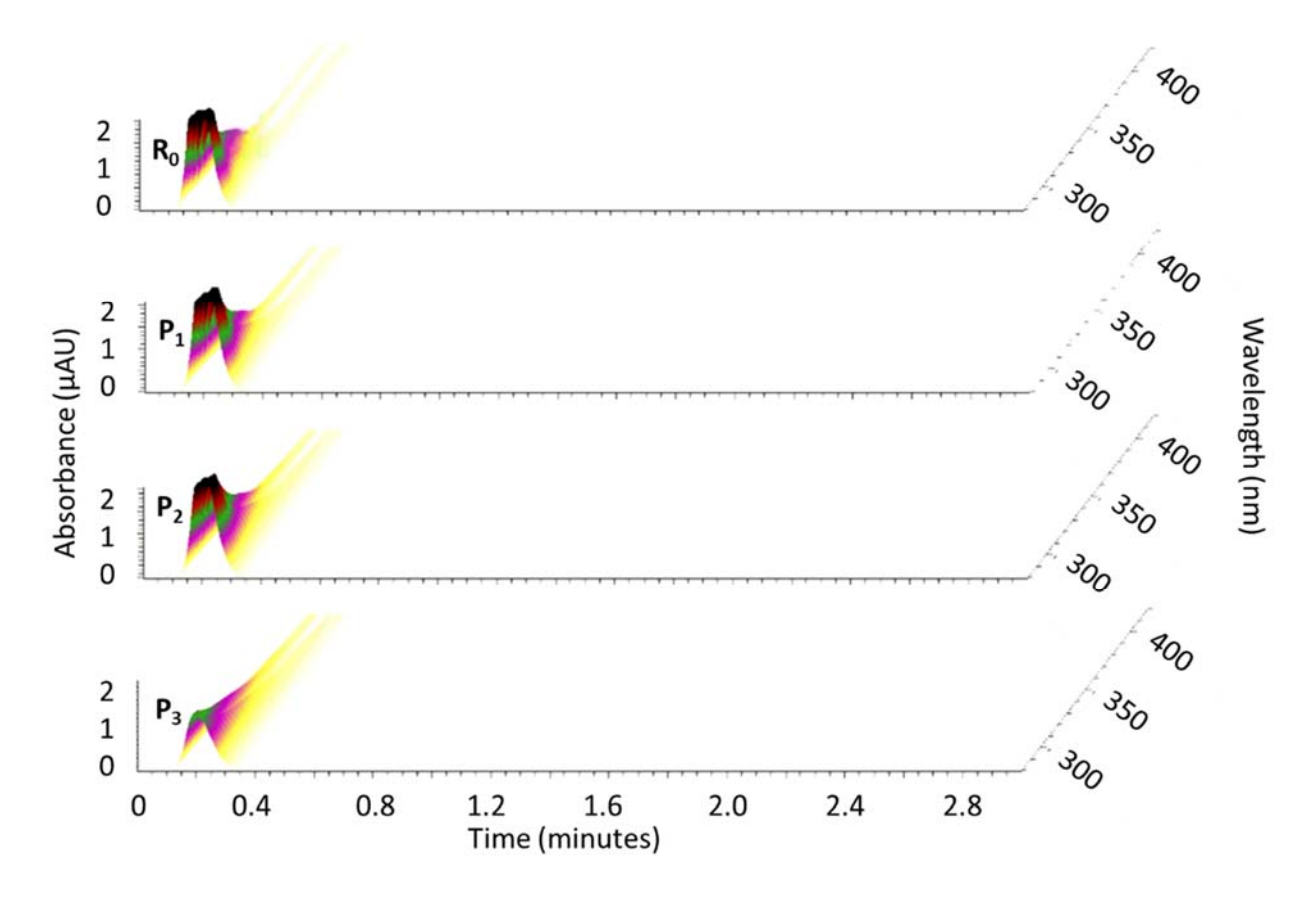


Figure S2. Column bypass runs for R_0 , P_1 , P_2 , and P_3 . Each plot was obtained by injecting the sample directly into the PDA cell without prior column separation.

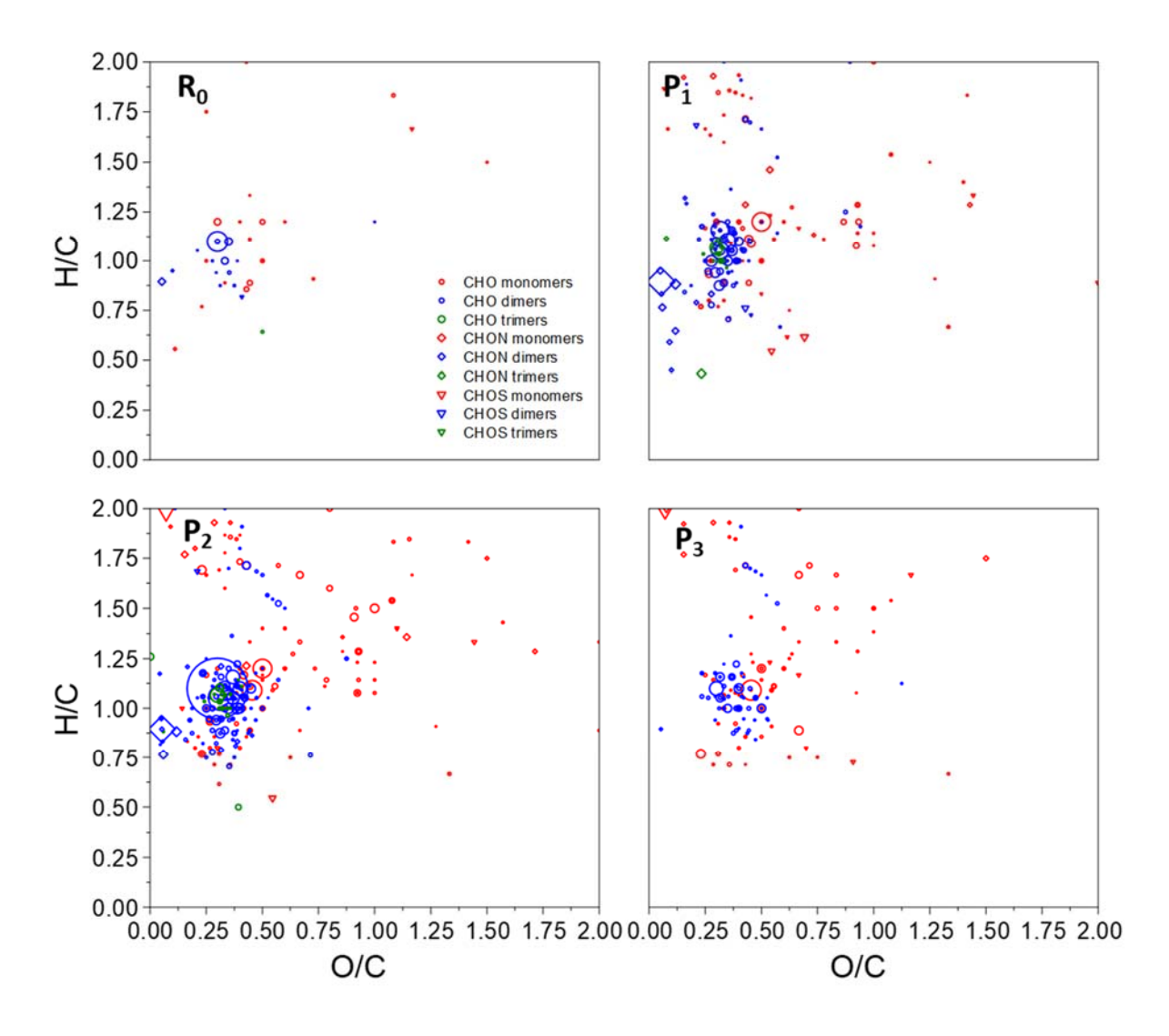


Figure S3. Van Krevelen plots for formulas assigned in the 3-30 minute region for R_0 (a), P_1 (b), P_2 (c), and P_3 (d). Size of individual symbols are scaled to cubic root of the HRMS signal intensity.

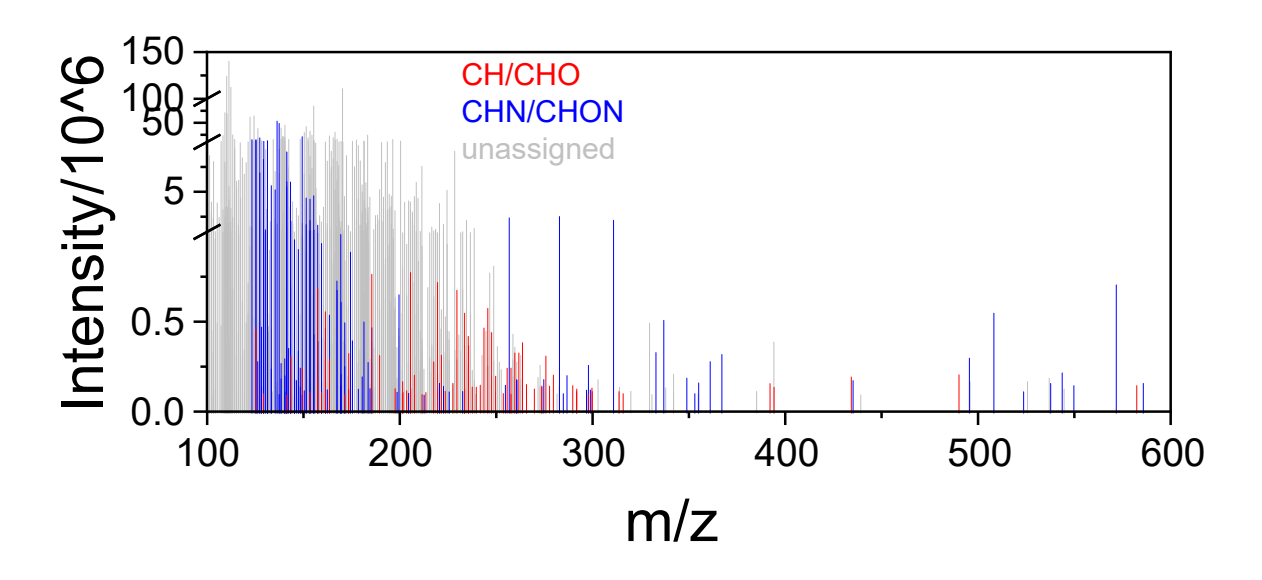


Figure S4. Positive mode mass spectrum collected between 60-103 min for P₃.

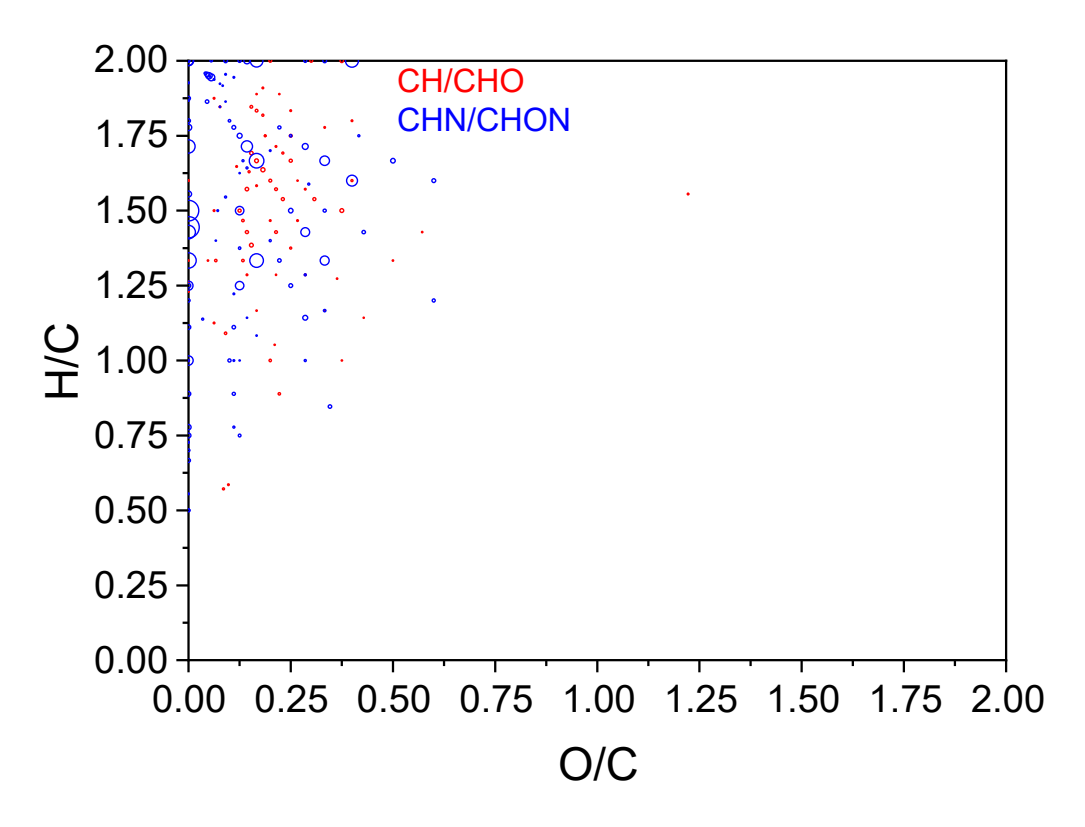


Figure S5. Van Krevelen diagram for formulas assigned in the 60-103 min region for P₃. Size of individual symbols are scaled to cubic root of the HRMS signal intensity.

Table S1. Chromophores detected in the GA+DMB system (note: a similar table is also found in Jiang et al¹)

#	UV-Vis spectrum and RT	Neutral Formula and Nominal Mass	Possible structures	Proposed Formation Mechanisms
1	RT = 8.8 - 9.6 min RT = 8.8 - 9.6 min 2 1 280 320 360 400	C ₇ H ₆ O ₃ 138.0317 amu	↓ OH	Formed by methoxy displacement ² of DMB. Both methoxy groups are replaced by hydroxyl groups
2	1.25x10 ³ 1.00 0.75 0.50 0.25 0.00 280 320 360 400	C ₈ H ₈ O ₄ , 168.0423 amu	но	Formed by methoxy displacement ² of DMB, followed by hydroxyl addition ³
3	2.0x10 ³ RT = 14.6 - 14.8 min 1.5 1.0 0.5 0.0 280 320 360 400	$C_{10}H_{12}O_6,$ 228.0634 amu	HO OH	Monomeric product of GA resulting from addition of three OH radicals ³ to the aromatic ring.
4	RT = 15.0 - 15.3 min RT = 2 280 320 360 400	C ₉ H ₁₀ O ₃ , 166.0630 amu	\$	DMB – the photosensitizer. Source of triplet carbon used to oxidize GA.
5	RT = 15.3 - 15.6 min	C ₁₀ H ₁₂ O ₃ , 180.0786 amu	Ů → → → →	GA – the phenol precursor.
6	RT = 16.3 - 16.6 min	C ₁₁ H ₁₂ O ₅ , 224.0685 amu	HO	Monomeric product of GA resulting from addition of an OH radical ³ and a methoxy radical ² to the aromatic ring. Another OH radical abstracts a proton, resulting in a water byproduct. ⁴ Rearrangement of double bonds to form a quinoidal system in conjugation with the ketone group.
7	RT = 19.8 - 20.0 min	C ₁₇ H ₁₈ O ₅ , 302.1154 amu		DMB+DMB dimeric product resulting from photolysis leading to the formation of CHO and dimethoxybenzyl radicals ⁵ and addition to an DMB unit. Hydrogen abstraction is then achieved by OH. ⁴
8	RT = 21.4 - 21.6 min 3 2 1 280 320 360 400	C ₁₉ H ₂₀ O ₆ , 344.1260 amu	OH OH	GA+DMB dimeric product formed by C-C linkage of a GA radical to a DMB unit. ³ Hydrogen abstraction is achieved by OH. ⁴

9	RT = 21.9 - 22.1 min 8 6 4 2 0 260 320 360 400	C ₂₀ H ₂₂ O ₇ , 374.1365 amu	OH OH	GA+GA dimeric product, formed by linking two C radicals; formed either before or after OH radical addition to one aromatic ring. ³
10	RT = 24.3 - 24.5 min RT = 24.3 - 24.5 min RT = 24.3 - 24.5 min RT = 24.3 - 24.5 min	C ₂₀ H ₂₂ O ₆ , 358.1416 amu	о С С С С С С С С С С С С С С С С С С С	GA+GA dimeric product, formed by linking two C radicals. ³
11	1.50x10 ³ 1.25 1.00 0.75 0.50 0.25 0.00 280 320 360 400	C ₁₉ H ₂₂ O ₆ , 346.1416 amu	HO HO	GA+GA dimeric product ³ resulting from Norrish photochemistry ⁶ with product 9. A CO unit is removed from the molecule.
12	2.0x10 ³ RT = 80.4 - 81.0 min 1.5 1.0 0.5 0.0 280 320 360 400	C ₁₁ H ₁₂ O 160.0888 amu		Pyrolytic-like product formed after extensive Norrish photochemistry. ⁶ Structure is chosen for its stability.
13	2.0x10 ³ RT = 94.4 - 94.8 min 1.5 1.0 0.5 0.0 280 320 360 400	C ₁₂ H ₁₂ 156.0938 amu	-	Pyrolytic-like product formed after extensive Norrish photochemistry. ⁶ Structure is chosen for its stability.

Scheme S1. C-O coupling of two GA radicals to form a GA dimer.

Appendix A. Calculation of AAE values from other studies

Our *AAE* values were calculated between 280-400 nm. Li et al⁷ calculated AAE values between 300-450 nm, and Chen et al⁸ calculated AAE values between 300-600 nm. To make a more accurate comparison with our work, their *AAE* values were recalculated using data points extrapolated from their plots in the 300-420 nm wavelength range using Matlab. Shik Park and Yu⁹ reported AAE values between 300-400 nm, so no additional calculation was performed. MAC₄₀₅ values from Li et al's⁷ study were extrapolated from their MAC plots using Matlab. Chen et al⁸ and Shik Park and Yu⁹ only reported MAC₃₆₅. MAC₄₀₅ was calculated using the relationship between MAC, wavelength and AAE¹⁰, and the calculated AAE values.

References

- (1) Jiang, W.; Misovich, M. V.; Hettiyadura, A. P. S.; Laskin, A.; McFall, A. S.; Anastasio, C.; Zhang, Q. Photosensitized Reactions of a Phenolic Carbonyl from Wood Combustion in the Aqueous Phase Chemical Evolution and Light Absorption Properties of AqSOA. *Environ. Sci. Technol.* **2021**.
- (2) Yee, L. D.; Kautzman, K. E.; Loza, C. L.; Schilling, K. A.; Coggon, M. M.; Chhabra, P. S.; Chan, M. N.; Chan, A. W. H.; Hersey, S. P.; Crounse, J. D.; Wennberg, P. O.; Flagan, R. C.; Seinfeld, J. H. Secondary Organic Aerosol Formation from Biomass Burning Intermediates: Phenol and Methoxyphenols. *Atmospheric Chem. Phys.* 2013, 13 (16), 8019–8043. https://doi.org/10.5194/acp-13-8019-2013.
- (3) Chen, Y.; Li, N.; Li, X.; Tao, Y.; Luo, S.; Zhao, Z.; Ma, S.; Huang, H.; Chen, Y.; Ye, Z.; Ge, X. Secondary Organic Aerosol Formation from 3C*-Initiated Oxidation of 4-Ethylguaiacol in Atmospheric Aqueous-Phase. *Sci. Total Enviornment* **2020**, *723*, 137953. https://doi.org/10.1016/j.scitotenv.2020.137953.
- (4) He, L.; Schaefer, T.; Otto, T.; Kroflic, A.; Herrmann, H. Kinetic and Theoretical Study of the Atmospheric Aqueous-Phase Reactions of OH Radicals with Methoxyphenolic Compounds. *J. Phys. Chem. A* **2019**, *123* (36), 7828–7838. https://doi.org/10.1021/acs.jpca.9b05696.
- (5) Theodoropoulou, M. A.; Nikitas, N. F.; Kokotos, C. G. Aldehydes as Powerful Initiators for Photochemical Transformations. *Beilstein J. Org. Chem.* **2020**, *16*, 833–857. https://doi.org/10.3762/bjoc.16.76.
- (6) Marchetti, B.; Karsili, T. N. V.; Ashfold, M. N. R. Exploring Norrish Type I and Type II Reactions: An Ab Initio Mechanistic Study Highlighting Singlet-State Mediated Chemistry. *Phys. Chem. Chem. Phys.* **2019**, *23* (26), 14418–14428. https://doi.org/10.1039/C8CP07292B.
- (7) Li, J.; Zhang, Q.; Wang, G.; Li, J.; Wu, C.; Liu, L.; Wang, J.; Jiang, W.; Li, L.; Fai Ho, K.; Cao, J. Optical Properties and Molecular Compositions of Water-Soluble and Water-Insoluble Brown Carbon (BrC) Aerosols in Northwest China. *Atmospheric Chem. Phys.* **2020**, *20* (8), 4889–4904. https://doi.org/10.5194/acp-20-4889-2020.
- (8) Chen, Y.; Ge, X.; Chen, H.; Xie, X.; Chen, Y.; Wang, J.; Ye, Z.; Bao, M.; Zhang, Y.; Chen, M. Seasonal Light Absorption Properties of Water-Soluble Brown Carbon in Atmospheric Fine Particles in Nanjing, China. *Atmos. Environ.* **2018**, *187*, 230–240. https://doi.org/10.1016/j.atmosenv.2018.06.002.
- (9) Shik Park, S.; Yu, J. Chemical and Light Absorption Properties of Humic-like Substances from Biomass Burning Emissions under Controlled Combustion Experiments. *Atmos. Environ.* **2016**, *136*, 114–122. https://doi.org/10.1016/j.atmosenv.2016.04.022 Get.
- (10) Srinivas, B.; Sarin, M. M. Light Absorbing Organic Aerosols (Brown Carbon) over the Tropical Indian Ocean: Impact of Biomass Burning Emissions. *Environ. Res. Lett.* **2013**, *8* (4), 044042. https://iopscience.iop.org/article/10.1088/1748-9326/8/4/044042.